J. Fluid Mech. (1976), *vol.* 76, *part* 2, *pp.* 307–336
Printed in Great Britain

The impingement of underexpanded axisymmetric jets on wedges

By P. J. LAMONT AND B. L. HUNT
Department of Aeronautical Engineering,
University of Bristol, England

(Received 19 November 1975)

This paper reports an experimental investigation into the impingement of underexpanded axisymmetric jets on each of three wedges arranged symmetrically in the jets. Three jets were used; two were produced by a convergent–divergent nozzle of exit Mach number 2·2 which was operated at underexpansion ratios of 1·2 and 2, while the third jet was produced by a convergent nozzle operated at an underexpansion ratio of 4. The base widths of the wedges equalled the exit diameter of the convergent–divergent nozzle, their apex angles were 90°, 60° and 45° and they were situated within or just downstream of the first cell of each jet.

Detailed front-face pressure distributions were obtained for 15 different configurations. Shadowgraph photographs were taken of these and other cases. The results show a variety of possible flow patterns. The major factors determining which flow pattern occurs are the combination of the centre-line Mach number and wedge apex angle and the jet shock strength and position. It was found that observed shock intersections can be reconstructed by means of shock polars, but that a four-shock confluence will not always occur when it is possible according to the shock polars. In one case there is evidence of the existence of a β triple-shock confluence. An interesting and unusual flow involving a stagnation bubble was obtained when the wedges were situated downstream of the free-jet Mach disk.

1. Introduction

The impingement of supersonic jets on various blunt obstacles, particularly flat plates, has been the subject of a number of previous studies, of which Donaldson & Snedeker (1971), Belov, Ginzburg & Shub (1973) and Carling & Hunt (1974) are recent examples. However, sharp-nosed devices, such as wedges, are often used as deflectors for rocket exhausts and have so far received very little attention by research workers. Although some theoretical work has been done on wedges in uniform, two-dimensional jets by Pack & Roberts (1953) and by Shifrin (1969, 1972), the authors are not aware of any investigations involving axisymmetric or non-uniform jets.

This paper reports an investigation into the impingement flow produced by underexpanded jets and three wedges of different apex angles. Each wedge was arranged symmetrically in the jet. The wedge-to-nozzle spacing was kept

relatively small, which is both realistic for a deflector and has the advantage that the flow is largely inviscid. The wedge base widths were comparable to the jet diameters, which is again realistic but leads to rather complex flow fields. Experimentally measured values of the surface pressure are presented along with the corresponding shadowgraph pictures of the flow fields. The main features are discussed and interpreted.

2. Experimental apparatus

Three supersonic jets were used in this work; two were produced by a convergent–divergent nozzle and the third by a convergent nozzle. The convergent–divergent nozzle had a conical exit section of 15° semi-cone angle designed to produce an exit lip Mach number M_E of 2·2. The exit diameter was chosen to be 30 mm to give as large a jet as possible consistent with a reasonable running time (at least 2 min) at the required operating pressures. The final entry contraction had a radius of curvature of 2·56 throat diameters. The initial expansion of the wall from the throat was a circular arc with radius equal to the throat diameter. The two jets from this nozzle were obtained by operating at those supply pressures which would give ratios of nozzle exit plane pressures p_E (based on the design value of M_E) to ambient pressure p_a of 1·2 and 2·0. The convergent nozzle had the same throat diameter as the convergent–divergent nozzle (21·4 mm) and the elliptic contour of the contraction was chosen so as to produce a nozzle of the same overall length as the convergent–divergent nozzle. The value of the underexpansion ratio p_E/p_a which was used with this nozzle was 4.

The rig used to supply the nozzles was rig II of Carling & Hunt's (1974) work, which brings air from a 30 bar main to the nozzle via an automatic control valve and a settling chamber. The pressure in the settling chamber is displayed on a Budenberg test gauge.

Three wedges were used in the tests, each having a base width of 30 mm, which is equal to the exit diameter D_E of the convergent–divergent nozzle; the wedges were 240 mm in length, which can be considered effectively infinite. The total apex angles were 90°, 60° and 45°. Under test, the wedges were mounted on a workshop machine table with compound cross-slides which formed part of the rig. The supports were arranged to be well clear of the jet so that no interference took place between the rig and the flow over the wedge. The cross-slides made it possible to centre the wedge accurately in the jet and to traverse it with precision parallel to its apex. This meant that a high resolution of surface pressure data parallel to the apex was possible. The resolution down the face of the wedge was limited to the spacing of the pressure tappings. The tappings were of 1·6 mm O.D. brass tubing and arranged in two rows 15 mm apart; the arrangement of the holes was such that a resolution of approximately one data point per 1·5 mm could be achieved by traversing both rows of pressure holes across the jet. In addition to the surface tappings, a Pitot tube of 0·8 mm O.D. was mounted in each wedge with its upstream end in line with the wedge apex. Initially, there was some doubt as to whether this tube would give an accurate measurement of the apex stagnation pressure: the results subsequently demonstrated that it did.

The surface pressures were measured with a 35 bar strain gauge transducer mounted in a Scanivalve unit. The digitized electrical output was recorded on paper tape and subsequently processed on the Department's Hewlett Packard 2100A computer.

A focused shadowgraph system was used to obtain photographs of the flow field. The system employed a conventional single-pass arrangement with a continuous light source.

Each wedge was carefully aligned with its base perpendicular to the jet and with its apex centrally located. The process of centralizing the wedge was accomplished by equalizing the readings from pressure holes at corresponding positions on opposite faces of the wedge.

3. The free jets

Since the impingement wedge positions were all relatively close to the nozzle, only the inviscid structure of the near jet is of importance. Even so, detailed information about the free jets is not easy to obtain. A reliable theoretical calculation of the flow would involve the use of an axisymmetric non-homentropic method of characteristics capable of computing the flow both in the nozzle and in the jet, and also capable of treating the jet shock by means of the Rankine–Hugoniot relations. On the other hand, it is very difficult to make reliable and detailed experimental measurements because of the small scale of the jet and because of the rapid variations in Mach number and flow direction. The development of either of these methods for the present work was not possible within the time available nor was it warranted by the scope of the investigation. Instead, information about the jets was obtained from approximate theoretical calculations in conjunction with a limited amount of experimental data.

The theoretical calculations were done by means of an axisymmetric, homentropic, method of characteristics program. This program is based on the method described by Vick *et al.* (1964). The program commences the calculation at the leading characteristic emanating from the nozzle lip. In the case of the sonic orifice, the flow upstream of this characteristic is approximated as parallel to the axis and having a Mach number of 1·0038: a value greater than unity is necessary to start the calculation. For the convergent–divergent nozzle, the flow upstream of the leading characteristic is assumed to be a radial source flow bounded by the conical walls of the nozzle. The characteristic equations used are axisymmetric but homentropic and no oblique shock relations are programmed for the jet shock wave. Instead, the so-called 'fold-back' technique is used whereby a characteristic is deleted each time a same-family crossing occurs. This means that the solution is isentropic, a shock wave location is predicted by the locus of the same-family crossings but flow quantities are continuous across this line although their derivatives are not. Naturally, such a technique cannot predict the position of the Mach disk.

The experimental investigation consisted of taking shadowgraph pictures of the free jets and of measuring centre-line Pitot pressures. A comparison of the shadowgraph pictures with the computed flow field shows good agreement

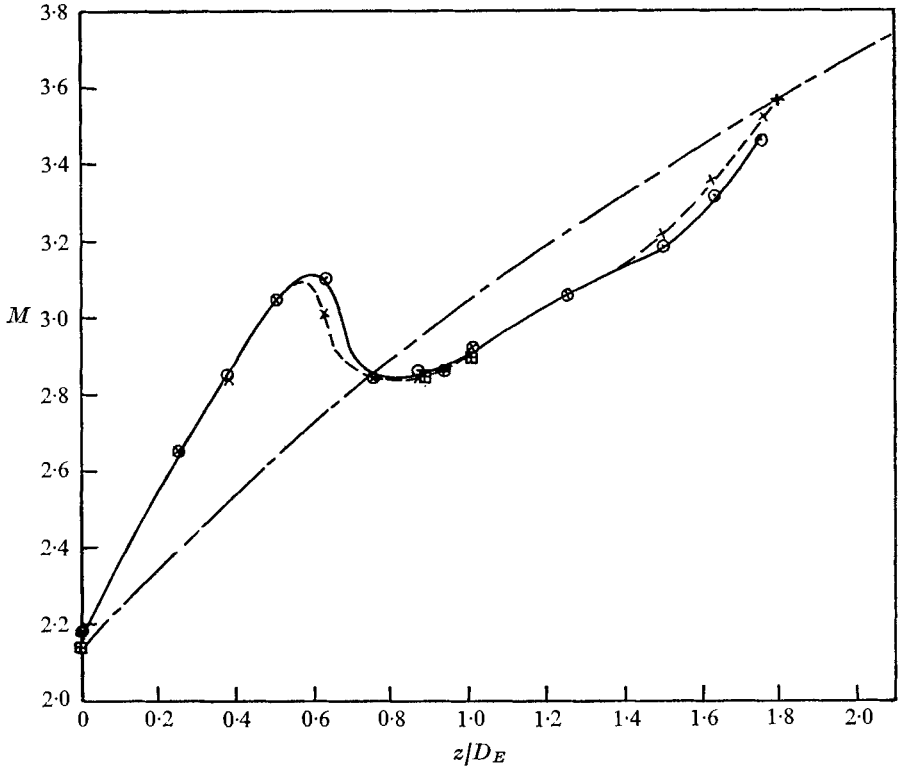

FIGURE 1. Mach number variation along the jet centre-line for the convergent–divergent nozzle. —⊙—, free-jet Pitot for $p_e/p_a = 1{\cdot}2$; - - - × - - -, free-jet Pitot for $p_e/p_a = 2{\cdot}0$; — · —, method of characteristics; ⊞, wedge apex Pitot for $p_e/p_a = 1{\cdot}2$; +, wedge apex Pitot for $p_e/p_a = 2{\cdot}0$ (two points, one of which is superposed on one of the points ⊙).

between the predicted and measured shock and jet-edge positions. For the convergent nozzle, the predicted centre-line Mach number distribution agrees well with the distribution deduced from the measured Pitot pressures: the theoretical distribution is of the correct shape but lies downstream of the experimental curve by approximately 0·1 nozzle exit radii. The centre-line Mach number distributions for the convergent–divergent nozzle are presented in figure 1. The discrepancy between the distributions shown on this figure cannot be ascribed to the homentropic assumption since the centre-line flow lies upstream of the jet shocks in this region. The error lies in the assumption about the nozzle exit flow, which is not truly radial in practice. Indeed, it can be seen that there is a rapid recompression in the actual jet; this is caused by a conical shock wave which originates at the nozzle wall, just downstream of the initial, circular-arc expansion region within which the flow overexpands. This nozzle shock wave can be seen in certain of the shadowgraph pictures, for example figure 3(*f*) (plate 2); it does not appear to have a substantial effect on the impingement flows.

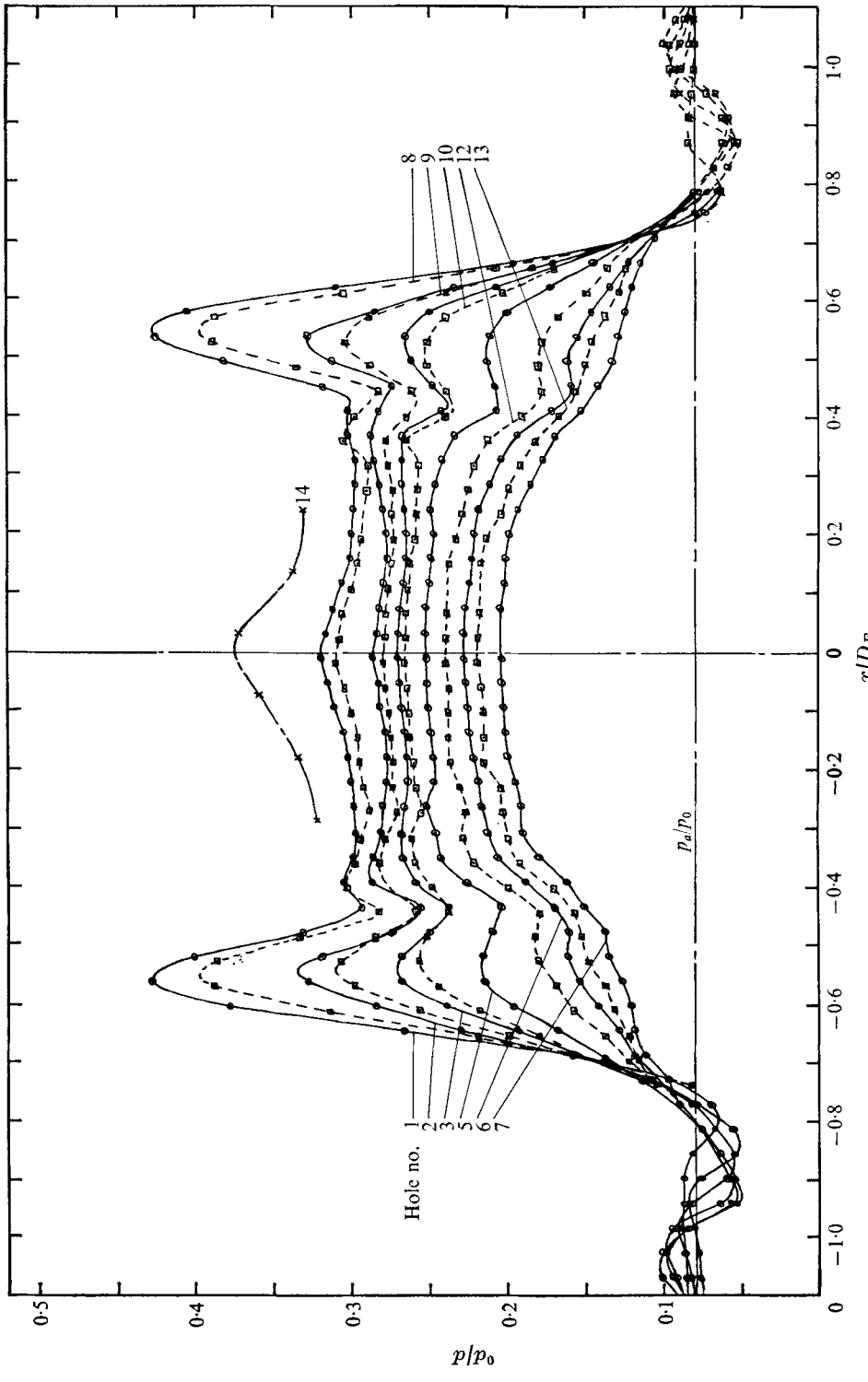

FIGURE 2. Surface pressures on the 90° wedge one diameter below the convergent-divergent nozzle for $p_e/p_a = 1{\cdot}2$.

Wedge apex angle	Separation distance divided by D_E	p_e/p_a	Figure showing contour plot	Figure showing centre-line distribution	Figure showing shadowgraph
		Convergent–divergent nozzle			
90°	0	1·2	15 (*a*)	10	3 (*a*)
		2·0	Not presented	Not presented	Not presented
	1	1·2	15 (*b*)	10	3 (*b*), (*c*)
		2·0	15 (*c*)	10	3 (*d*), (*e*)
	2	1·2	15 (*d*)	13	3 (*f*), (*g*)
		2·0	15 (*e*)	10	3 (*h*), (*i*)
60°	0	1·2	16 (*a*)	11	4 (*a*)
	1	1·2	16 (*b*)	11	4 (*b*)
		2·0	—	11	4 (*c*)
	2	1·2	16 (*c*)	13	4 (*d*), (*e*)
		2·0	—	—	4 (*f*), (*g*)
45°	0	1·2	17 (*a*)	12	5 (*a*)
	1	1·2	17 (*b*)	12	5 (*b*)
		2·0	—	12	5 (*c*)
	2	1·2	17 (*c*)	13	5 (*d*), (*e*)
		2·0	—	—	5 (*f*), (*g*)
		Convergent nozzle			
90°	0	4	18 (*a*)	14	6 (*a*)
	1	4	18 (*b*)	14	6 (*b*), (*c*)
	2	4	18 (*c*)	14	6 (*d*), (*e*)

TABLE 1

4. Presentation of the results

A total of fifteen complete distributions of surface pressure on the wedge were obtained, mainly using the convergent–divergent nozzle. The results are presented as values of the absolute pressure p divided by the nozzle chamber pressure p_0. An example of a distribution is shown in figure 2. This figure allows the quality of the experimental results to be judged. However, a detailed interpretation can be made only if the exact location of each hole is tabulated. Furthermore, most of the distributions are more complex than that shown in figure 2 and the corresponding figures are very difficult to decipher. The pressure distributions are therefore presented as contour plots in figures 15–18. In these figures, x is the distance parallel to the wedge apex measured from the centre-line and s is the perpendicular distance from the apex measured along the wedge surface. The plot for the 90° wedge at zero spacing ($z_w = 0$) below the convergent–divergent nozzle at a pressure ratio of 2 is virtually identical to figure 15 (*a*) except in the outermost region and is therefore omitted. Dashed lines on the contour plots represent extrapolated results. In making these extrapolations, use was made of features from the shadowgraph pictures (figures 3–7, plates 1–10): such features are indicated on the contour plots.

The distributions of pressure down the centre-line of the wedges are presented in figures 10–14. Figures 10, 11 and 12 contain the pressure variations for the convergent–divergent nozzle with the 90°, 60° and 45° wedges respectively, except that certain anomalous distributions have been omitted and are plotted together on figure 13. The curves for the convergent nozzle with the 90° wedge are shown on figure 14. Where the stagnation pressure is known along these distributions, the Mach number has been calculated and is shown. In most of the figures, the points shown are values for each wedge pressure hole interpolated from distributions of the type shown in figure 2. Because of the high resolution parallel to the apex, these values are very nearly as reliable as directly measured experimental points. The curves shown for the 60° and 45° wedges at one diameter separation using the higher pressure ratio were obtained by direct measurement along the centre-line. (Full pressure surveys were not taken in these cases.) Also shown on figures 10–14, where appropriate, are values of the Pitot pressure p_{01} measured on the centre-line of the free jet at the location of the wedge shock (as determined from the corresponding shadowgraph picture), values of the wedge pressure p_w from simple, two-dimensional oblique shock theory using the Mach number on the centre-line of the free jet at the location of the wedge apex, and the positions of shock waves which impinge on the wedge surface (again taken from the shadowgraphs).

Shadowgraph pictures were taken parallel to the apex in every case investigated and also perpendicular to the apex in cases where the wedge shock is detached. Shadowgraph pictures are presented in figures 3–6 for all the cases studied, with the exception of the wedges at zero spacing for an underexpansion ratio of 2: these pictures are virtually indistinguishable from those taken with the lower pressure ratio.

The case studied are tabulated for reference in table 1.

5. Discussion of the results

The results are discussed in the following manner. The shock shapes, as seen on the shadowgraph pictures, are considered first because they have a major influence on the surface pressures. Then because the centre-plane flow is easier to study than flow in off-centre planes, the centre-line pressure distributions are discussed. The contour plots are considered next and, finally, a complex and interesting flow which occurs in certain cases is discussed in detail.

5.1. *Shock shapes*

The shadowgraph photographs show an interesting variety of flows. In studying them, it should be remembered that, although the optical system was focused near the centre-plane and most of the observable features occur in this plane, the finite depth of focus reveals some non-central features also.

In all cases except that of figure 6(*a*) (plate 7) the wedge produces a shock wave which, in turn, intersects the jet shock. Both the form of the wedge shock and the nature of the intersection can vary considerably. Examples are presented of all of the following: wedge shock detached and highly convex upwards (figure

3*a*, plate 1), wedge shock detached and concave upwards (figure 3*h*, plate 2), strong attached wedge shock (figure 4*b*, plate 3), weak attached wedge shock (figure 5*a*, plate 5), a four-shock intersection point (figure 5*c*, plate 5), a single three-shock intersection point (figure 5*f*, plate 6), and two three-shock intersection points (figure 5*b*, plate 5). Furthermore, it can be seen that the shock curvatures are not necessarily of the same nature for both the points of view from which the photographs were taken.

At a separation distance of $2D_E$ in the jet of lower pressure ratio from the convergent–divergent nozzle and in the jet from the convergent nozzle, the wedge apex is downstream of the free-jet Mach disk. It can be seen from figures 3(*f*), 4(*d*), 5(*d*) and 6(*d*) (plates 2, 4, 6 and 8) that the shock structure retains the characteristic Mach-disk shape, although the central shock is displaced slightly upwards by the wedges, whose presence is signalled upstream through the subsonic part of the flow. The distances of the Mach disk below the convergent–divergent nozzle are 1·72 nozzle diameters for the free jet and 1·64, 1·6 and 1·57 diameters for the 45°, 60° and 90° wedge respectively. For the convergent nozzle, the presence of the 90° wedge raises the Mach disk from 1·75 to 1·63 nozzle diameters from the nozzle.

In the bulk of the remaining cases, where the apex is upstream of the free-jet Mach disk, it is natural to inquire whether simple oblique shock theory using the centre-line Mach number will correctly predict whether the wedge shock is attached or detached at the apex. It turns out that a detached shock always occurs when one is predicted but, of the seven cases where an attached shock is predicted, two have detached shocks (see figures 4*f* and 5*f*, plates 4 and 6) and one has a strong attached shock (see figure 4*b*, plate 5). A simple centre-line deflexion criterion is therefore not sufficient to determine whether or not the shock is attached although, in cases where a weak attached shock occurs, the measured shock angle at the apex agrees well with the oblique shock prediction.

It can be seen from the shadowgraphs that the jet pressure ratio can have a powerful influence on the shock patterns. For example, figures 4(*b*) and (*c*) (plate 3) show the effect of increasing the pressure ratio for the 60° wedge at one diameter spacing; note that the change in pressure ratio leaves the centre-line Mach number unaltered. It can be seen in figure 4(*b*) that, at the lower pressure ratio, a strong shock wave occurs, probably attached to the wedge apex. On the other hand, at the higher pressure ratio, illustrated in figure 4(*c*), the wedge shock is weak and attached at the apex. The interaction of this wedge shock with the jet shock has a somewhat complex structure involving two three-shock confluence points separated by a section of strong shock wave. This basic shock structure has been observed previously by Edney (1968) as part of his excellent study of shock impingement; Edney classifies it as a type II interaction in his work; here it will be referred to as a 'double triple point'. A double triple point can also be seen above the 45° wedge at the lower pressure ratio (figure 5*b*, plate 5); at the higher pressure ratio, the jet shock and the wedge shock of the 45° wedge meet in a four-shock confluence point (see figure 5*c*, plate 5). The main effect of a change in pressure ratio is to change the strength and position of the jet shock; it is clear from the above that these quantities can play a major part in determining

the structure of the shock system. Additional shadowgraphs were therefore taken of the 60° and 45° wedges at one diameter separation over a wider range of pressure ratios. The results for the 45° wedge at pressure ratios of from 0·8 to 2·3 are presented in figure 7 (plates 9 and 10). It can be seen that raising the pressure ratio from 0·8 to 2·3 produces a change in the shock structure according to the following sequence: detached shock, strong attached shock, double triple point and four-shock confluence. The shock structure on the 60° wedge followed the same sequence.

The flows studied by Edney (1968) were produced by the impingement of a simple wedge shock on various points along the stand-off shock produced by a blunt body in an otherwise uniform supersonic stream. Edney's flow was therefore asymmetric, unlike ours. A number of the shock intersection patterns which he observed can exist only in an asymmetric situation and would not therefore be expected to occur in our case. However, the four-shock confluence and the double triple point occur in both flow fields. Edney found that both types of intersection point could be correctly reproduced by means of shock polar constructions. In the present case, such constructions can only be approximate since the jet shock strength and complete jet flow field are not known accurately. The approach adopted was to measure the shock angles from the shadowgraphs and to obtain the upstream Mach number and flow direction from the method of characteristics solutions. The shock polar construction for figure 5(*c*) (plate 5) is qualitatively the same as shock polars I, II and III of figure 8(*b*), which will be discussed shortly: the existence of a four-shock confluence is correctly predicted and the predicted values of the transmitted shock angles agree well with the measured values. In the case of figure 5(*b*), the extrapolated situation where the free-jet shock wave intersects the wedge shock in a four-shock confluence point was reconstructed in order to see if the shock polars allow such a confluence point. The shock polars again turned out to be very little different from polars I, II and III of figure 8(*a*). A four-shock intersection is therefore present on the polars, in disagreement with the double triple point which occurs in figure 5(*b*) (plate 5). Furthermore, the extent of the overlap of the transmitted jet and wedge shock polars is large and means that the discrepancy cannot be ascribed to the approximations made in the shock polar diagram. Indeed, the shock polar diagrams are generally found to be insensitive to both the measured shock angles and the calculated flow conditions.

A closer study of figure 7 (plates 9 and 10) provides an explanation for the occurrence of the double triple point in preference to the four-shock confluence. It can be seen in figure 7 (*g*) that the transmitted section of the jet shock impinges on the wedge surface and causes the boundary layer to separate. Separation occurs upstream of the inviscid impingement point and produces an oblique separation shock which then intersects the transmitted jet shock. In figure 7 (*g*) this intersection appears to be in the form of a four-shock confluence. As the supply pressure is lowered, however, the separation point moves up the wedge and the intersection of the jet and separation shocks becomes a double triple point (see figures 7*f*, *e*). As this shock structure moves up the wedge, the extent of the transmitted part of the jet shock decreases and the outer triple point moves

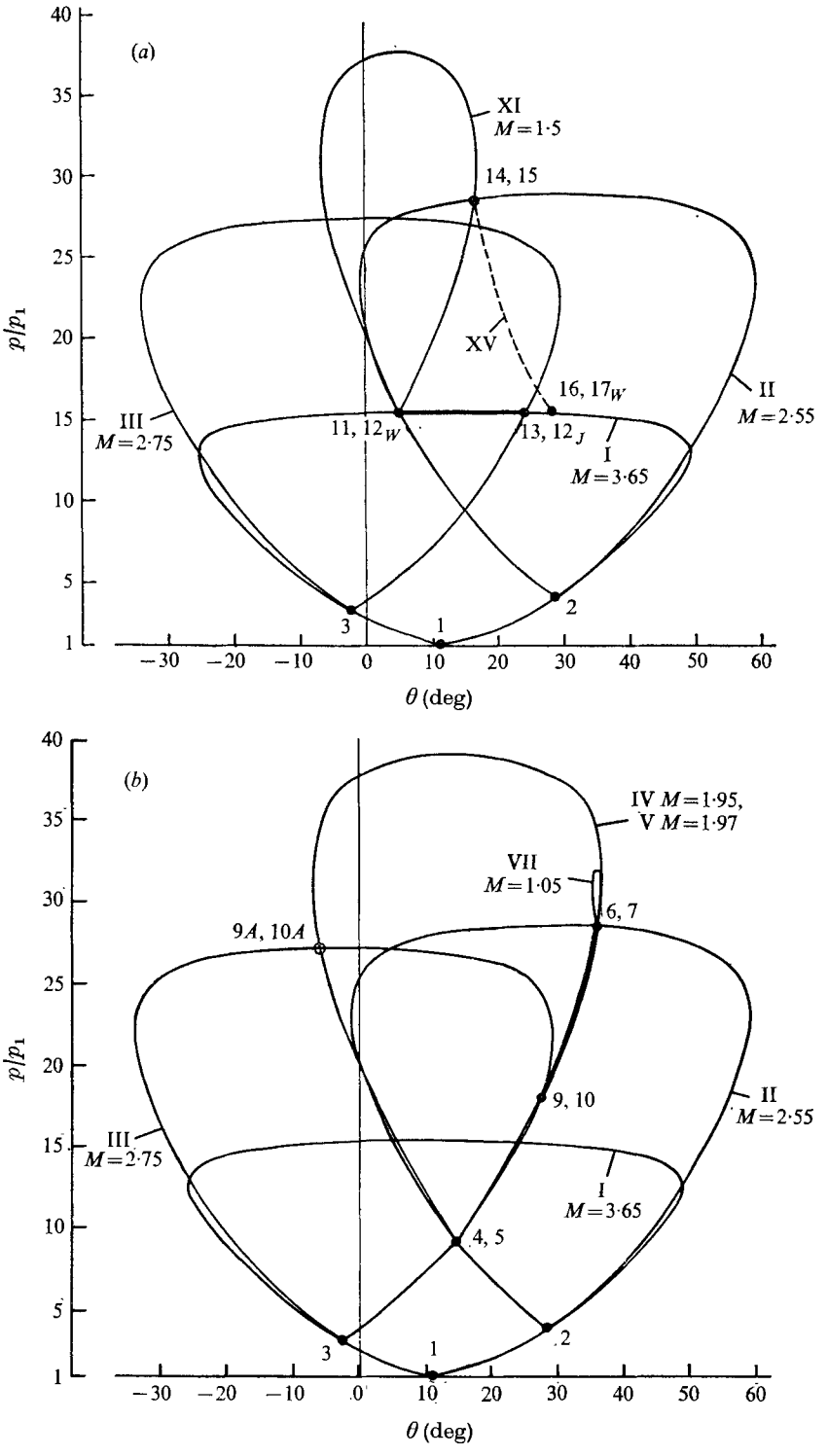

FIGURE 8. Shock polar diagrams (*a*) for the flow in figure 7 (*d*) and (*b*) for the flow in figure 7 (*e*).

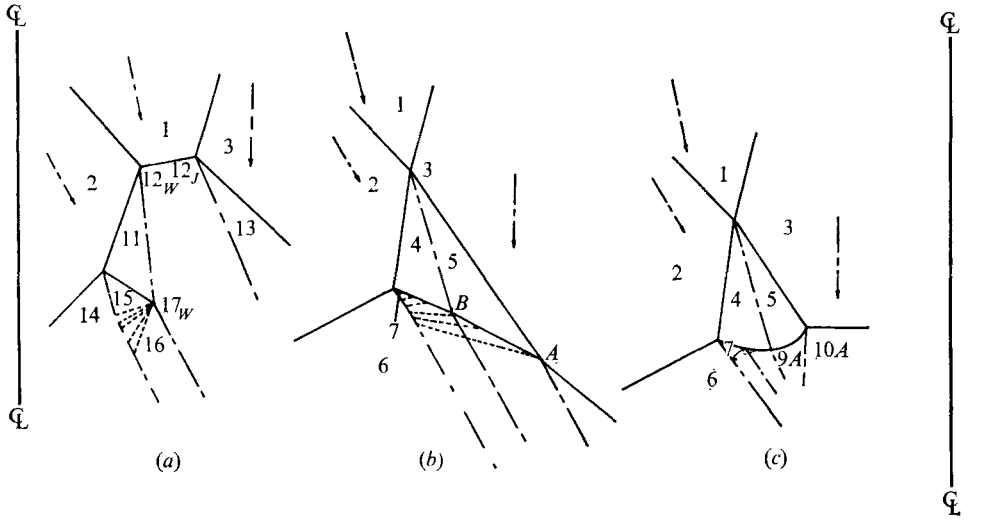

FIGURE 9. Physical-plane diagrams (*a*) for the flow in figure 7 (*d*), (*b*) for the flow in figure 7 (*e*) and (*c*) for the alternative solution to figure 7 (*e*).

towards the wedge and jet shock intersection point. The shadowgraphs in figures 7 (*e*) and (*d*) suggest that the change from a four-shock intersection to a double triple point configuration occurs when the outer triple point of the separation and jet shock intersection reaches the wedge and jet shock intersection. Since the two confluence points cannot coincide, the jet and wedge shock intersection changes its structure into the double triple point of figure 7 (*d*). This structure lies further upstream than the original four-shock confluence while the separation point does not move significantly; this allows the tail shock from the wedge shock triple point to establish a second double triple point with the separation shock as seen in figure 7 (*d*). Details of the two flow patterns can be constructed by means of shock polar diagrams. Figures 8 and 9 show the flow patterns in both the shock polar and physical planes. In these diagrams, the upstream flow in region 1 has been taken as constant. The Mach number and flow direction are those given by the method of characteristics solution at the position of the four-shock confluence in figure 7 (*e*). The wedge and jet shock angles were measured at the four-shock confluence of the same figure. The angles in the diagrams of the physical plane were obtained from the shock polar diagrams: the length scales are arbitrary. It can be seen that the reconstructed flow patterns in figures 9 (*a*) and (*b*) agree well with the corresponding regions of figures 7 (*d*) and (*e*). The bow shock angles at the two triple points of figures 8 (*a*) and 9 (*a*) are not equal and, consequently, the conditions at points 12_W and 12_J are different. This means that the two triple points will be a finite distance apart even on the initial occurrence of the double triple arrangement: the transition between the two structures must therefore be a discontinuous one. It is thus not obvious that the transition will occur at the same operating pressure when this pressure is rising as it does when it is falling. Several attempts were made to investigate this point but the degree of control required was beyond the capability of the apparatus.

The reconstruction of the shock configuration for the four-shock confluence (figures 8*b*, 9*b*) raises an interesting point of detail concerning the intersection of the shock waves terminating regions 3 and 5. Conditions in region 7 are barely supersonic and shock polar VII of figure 8(*b*) does not intersect shock polar III, hence making a four-shock intersection impossible. In such a case, a possible solution is for shock polars IV and VII to form a triple-point confluence, in this case involving a Guderley patch as described by Henderson (1965) for example, and for the bow shock to turn and form a second triple point with shock polar III. This point is shown by an open circle on figure 8(*b*). The corresponding physical-plane diagram is shown in figure 9(*c*). However, the shock and slip-line angles are at variance with those to be seen in figure 7(*e*) (plate 10); one is therefore led to look for another solution. Such a solution can be constructed if it is supposed that the right-hand intersection of shock polars V and III occurs. This is a β intersection in the terminology adopted by Henderson (1965). For this intersection to be possible, shock 4–7 must weaken as it is propagated towards shock 3–5. This weakening can be accomplished if the slip line which eventually separates regions 6 and 8 of figure 9(*b*) first turns and emits expansion waves. The information necessary for the correct degree of turning to be achieved can be transmitted to region 6 from point A (or possibly point B) of figure 9(*b*) and hence passed upstream in region 6, which is subsonic, to the relevant section of the slip line. Figure 9(*b*) was constructed using angles derived from the shock polars of figure 8(*b*). It can be seen that the shock and slip-line angles are in agreement with those of figure 7(*e*). Varying the shock angles and flow conditions used to construct figures 8 and 9 by small amounts produces only small changes in the diagrams and confirms that the agreement obtained from the β intersection is not just fortuitous. If correct, this is particularly interesting since we are not aware of any previous observation of a β intersection: Kalghatgi & Hunt (1975) concluded that β intersections were virtually impossible for over-expanded jets impinging on flat plates while Henderson (1965) had previously reached the same conclusion for unseparated flow on wedge intakes although he pointed out that they may occur if the wedge flow separates.

Returning to the sequence of events as the pressure ratio falls in figure 7, after a double triple point has been formed the width of the subsonic flow region increases as the nozzle pressure ratio falls. This causes the inner triple point to move up the wedge shock until it reaches the apex. A strong attached shock is first formed and then detaches as the pressure ratio is further reduced. The detached-shock cases at two diameter spacing with the 60° and 45° wedges shown in figures 4(*f*) and 5(*f*) correspond to this last point in the sequence: it was confirmed by observing the shadowgraph image for these configurations that the wedge shock became attached at high supply pressures.

Shock polars were constructed for most of the recorded shock intersection points. They were found to agree well with the observed features.

5.2. *Centre-line pressures*

The centre-line pressure distributions presented in figures 10–14 can be related to values of the Mach number wherever the total pressure on the centre-plane

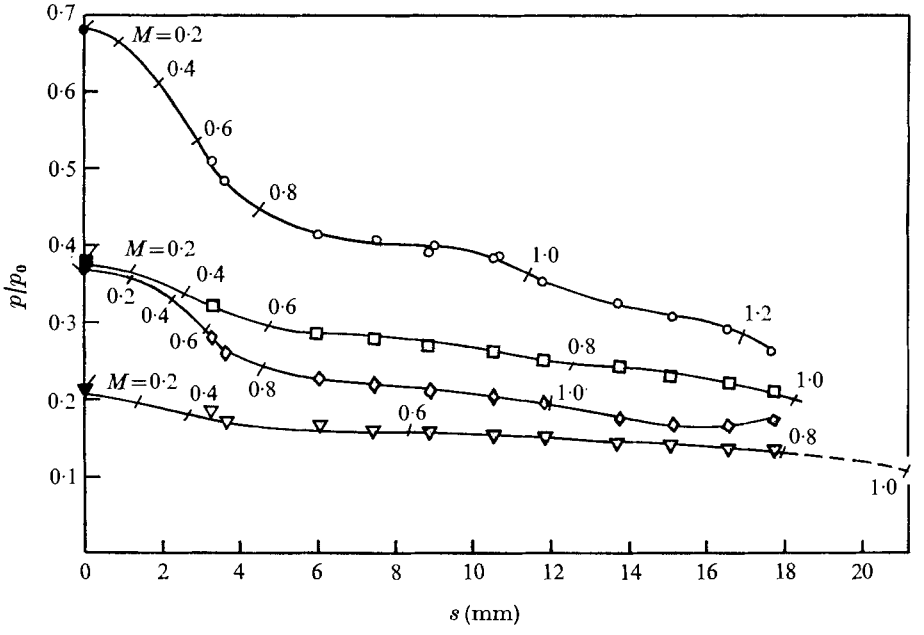

FIGURE 10. Centre-line pressures for the 90° wedge below the convergent–divergent nozzle. ○, $z_w = 0$, $p_e/p_a = 1·2$; □, $z_w = D_E$, $p_e/p_a = 1·2$; ◇, $z_w = D_E$, $p_e/p_a = 2·0$; ▽, $z_w = 2D_E$, $p_e/p_a = 2·0$. Flagged symbols, apex Pitot values; solid symbols, free-jet Pitot values.

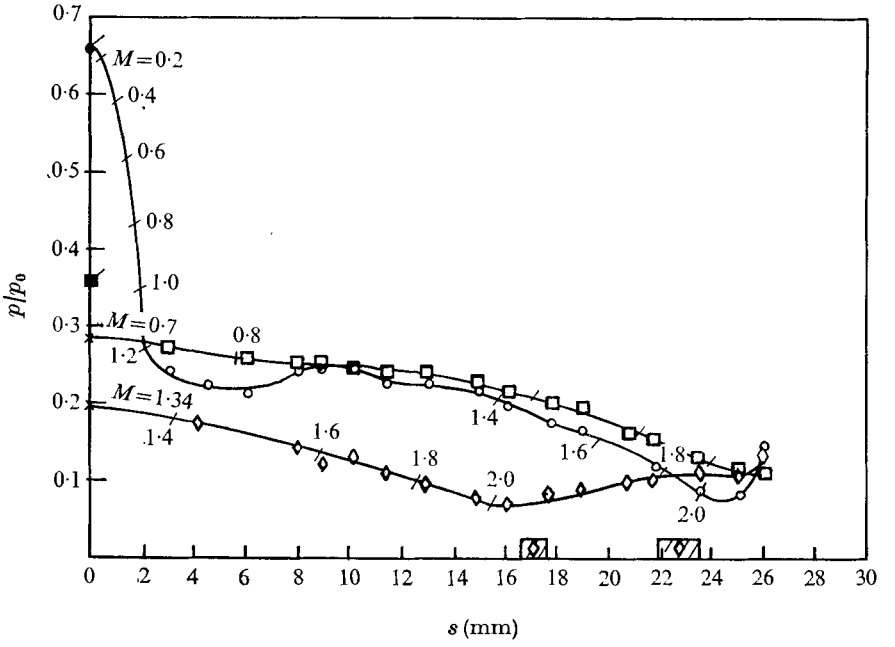

FIGURE 11. Centre-line pressures for the 60° wedge below the convergent–divergent nozzle. ▨, shock position taken from shadowgraph; ×, value from oblique shock theory. For remaining symbols see figure 10.

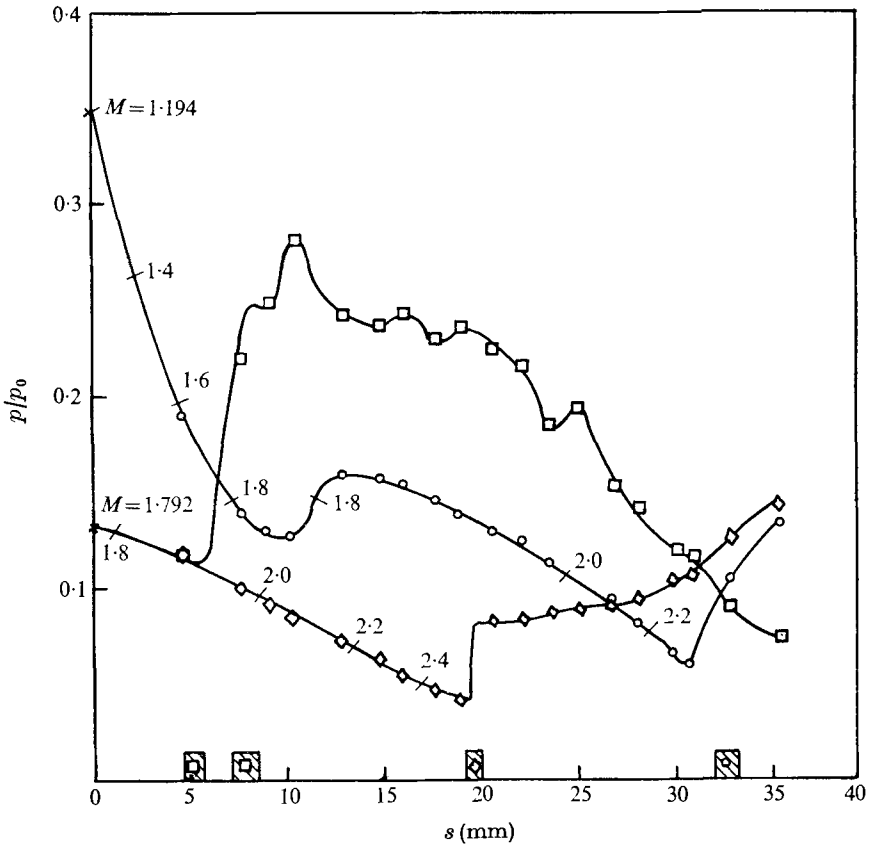

FIGURE 12. Centre-line pressures for the 45° wedge below the convergent–divergent nozzle. For symbols see figure 11.

streamline remains constant. They can mostly be interpreted with the aid of the corresponding shadowgraphs.

In cases where the shadowgraphs show the wedge shock to be attached, the surface pressures are extrapolated to meet the apex value p_w predicted by oblique shock theory. In the case of the 60° wedge at one diameter separation and the lower pressure ratio (see figure 11), p_w was calculated from the strong oblique shock solution since the shadowgraph appears to show a strong attached shock at the wedge apex. In every case (including this strong shock case), the extrapolation can be carried out smoothly, indicating that p_w is the correct apex value. Where the wedge shock is detached, the value recorded from the wedge Pitot probe is consistent with the surface tappings and may be taken to be the true apex value. In most cases, this value is in agreement with the corresponding value of p_{01}, the free-jet Pitot pressure at the central point of the wedge shock. There are four exceptional cases, all of which occur when the wedge is below the free-jet Mach disk; three are plotted together in figure 13 and the fourth is the lower curve of figure 14. These cases are discussed in detail in § 5.4.

The detached-shock cases mostly have centre-line pressure distributions which fall from the Pitot pressure at the apex to a sonic or slightly supersonic value at

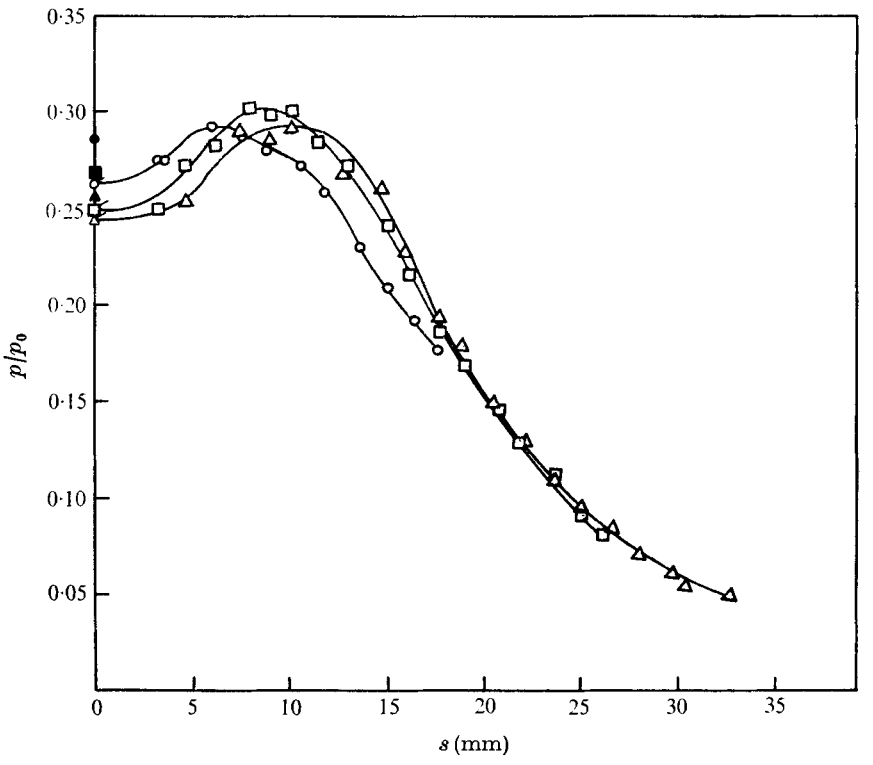

FIGURE 13. Centre-line pressures for the wedges at $z_w = 2D_E$ below the convergent–divergent nozzle with $p_e/p_a = 1{\cdot}2$. ○, 90° wedge; □, 60° wedge; △, 45° wedge. Flagged symbols, apex Pitot values; solid symbols, free-jet Pitot values.

the base. The pressure gradient tends to decrease as the upward concavity of the wedge shock increases. Compare, for example, the top and bottom curves of figure 10, for which the shadowgraphs are figures 3(*a*) and (*h*) (plates 1 and 2). The 60° wedge at zero spacing has a detached shock but the wedge angle is very close to the shock detachment angle, as can be seen on figure 4(*a*) (plate 3). Moreover, the upstream flow angle increases away from the centre-line, reducing the effective deflexion angle. Consequently this flow behaves very much like an attached-shock case. The central pressures are shown on figure 11; they drop extremely rapidly close to the apex and then fall much more slowly until the shock which is transmitted from the four-shock confluence impinges on the wedge just upstream of the final pressure tapping, causing a sudden increase in pressure. The earlier rise in pressure in this curve, which begins about 6 mm from the apex, is probably due to the weak nozzle shock waves mentioned in § 3: a reconstruction of their likely point of impingement on the wedge surface put this point at 7 mm from the apex. A similar rise in pressure can be seen on the pressure distribution for the 45° wedge at zero spacing (figure 12). In the case of the 90° wedge at zero spacing, the nozzle shocks intersect the wedge shock in a region where the downstream flow is subsonic and, consequently, the upper curve of figure 10 does not contain a shock-induced pressure rise.

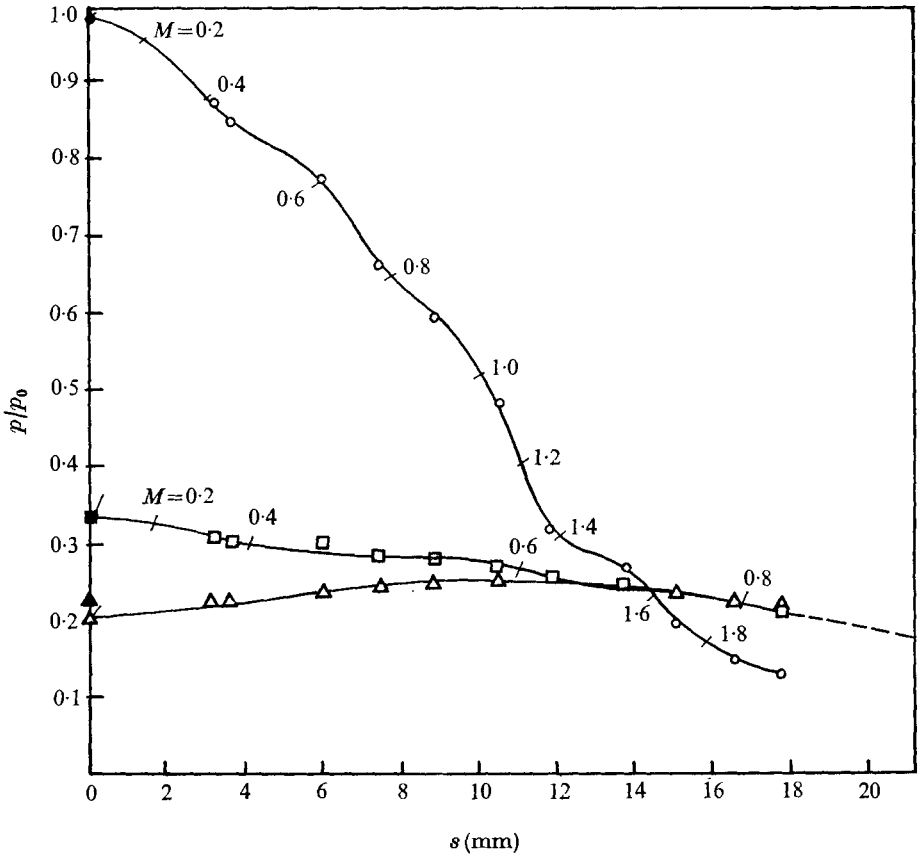

FIGURE 14. Centre-line pressures for the 90° wedge below the convergent nozzle with $p_e/p_a = 4$. ○, $z_w = 0$; □, $z_w = D_E$ (where D_E is the exit diameter of the convergent–divergent nozzle); △, $z_w = 2D_E$.

In every case where the wedge shock is attached and weak at the apex the interaction of the jet and wedge shocks results in a shock wave impinging on the wedge surface. The locations of these impingement points as determined from the shadowgraphs are shown on the centre-line pressure distributions: these locations can be seen to agree well with the positions of the measured pressure rises. In the region between the apex and an impinging shock, the pressure falls (see for example figure 12). A possible explanation for this is the following. As one moves away from the apex along the wedge shock, approximate calculations show that the static pressure just downstream of the shock decreases while the flow angle remains roughly parallel to the wedge. If all the streamlines between the wedge and the shock are also parallel to the wedge, the static pressures along a line normal to the wedge surface must be constant and, hence, the surface static pressure must fall on moving away from the apex. For example, if one takes a point on figure 5 (*c*) just upstream of the point where the shock impinges on the surface, then the estimated values of the non-dimensional static pressure and flow direction at the shock point which lies on the normal from this surface point

are 0·035 and 23° respectively, compared with 0·04 and 22·5° at the surface point, the surface pressure having fallen from 0·13 at the apex.

The two cases which arise from double triple point shock structures may be found on figures 11 and 12. In the flow over the 60° wedge, the shock from the inner triple point impinges on the surface about half-way down the wedge and only part of the wave pattern which can be seen in figure 4(*c*) influences the pressure-tapped region. In the case of the 45° wedge, only a short length of weak attached shock occurs before the first triple point. The resulting tail shock impinges on the surface and produces the steep rise in pressure seen on figure 12. The shadowgraph of this case (figure 5*b*, plate 5) shows evidence of a number of wave reflexions occurring between the wedge surface and the slip line which originates from the triple point. It is presumably these waves which produce the irregularities in the generally falling pressure distribution over the remaining part of the wedge.

Finally, it can be seen from figure 14 that, when the 90° wedge was placed with its apex in the exit plane of the convergent nozzle, the apex pressure was nearly equal to the nozzle supply pressure. This is to be expected since no wedge shock can occur in this case. Further down the wedge, the flow accelerates rapidly and leaves the trailing edge at somewhat over Mach 2·0. The supersonic part of this acceleration is due to expansion waves which originate at the nozzle lip. These waves are transmitted through the flow and reflected from the wedge surface.

5.3. *Pressure contours*

The reliability of the pressure measurements is generally felt to be very satisfactory. The spatial resolution achieved by traversing the wedges was excellent and that down the wedge surfaces was adequate, even when the occasional reading was lost in testing. The readings from corresponding holes on either side of the apex agreed within plotting accuracy. The pressure distributions were generally very symmetric about the centre-plane, as can be seen in figure 2. The apex pressure tube, about which some concern had been felt, gave readings which were in very good agreement with the free-jet Pitot pressures (see figure 1) and in all detached-shock cases gave readings entirely consistent with the surface tappings.

It can be seen from the contour plots that the main region of high pressure on the wedge occurs approximately within the span of the free jet. In most cases, the distribution along the wedge under the central part of the jet is fairly uniform but substantial pressure peaks occur in the outer part of the flow in cases where the wedge is at some distance from the nozzle. The expansion of the edge streamline can be clearly seen in all the contour plots. (Values of p_a/p_0 for the jets from the convergent–divergent nozzle are 0·078 for $p_e/p_a = 1{\cdot}2$ and 0·047 for $p_e/p_a = 2$; for the jet from the convergent nozzle, $p_a/p_0 = 0{\cdot}132$.) In the outermost regions there is evidence of overexpansion and recompression which may be a weak form of the wall-jet wave behaviour described by Carling & Hunt (1974) for a perpendicular flat plate. When the apex is at some distance from the nozzle, a slip line originates from the triple point and gives rise to another expansion region which is most extensive at the larger separation distances, where the jet shock is strongest.

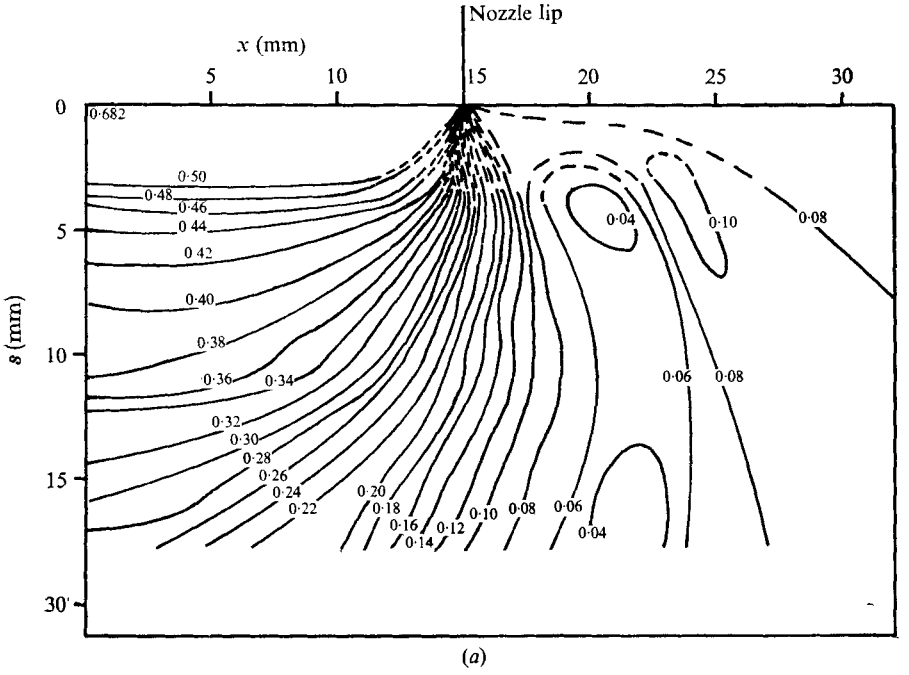

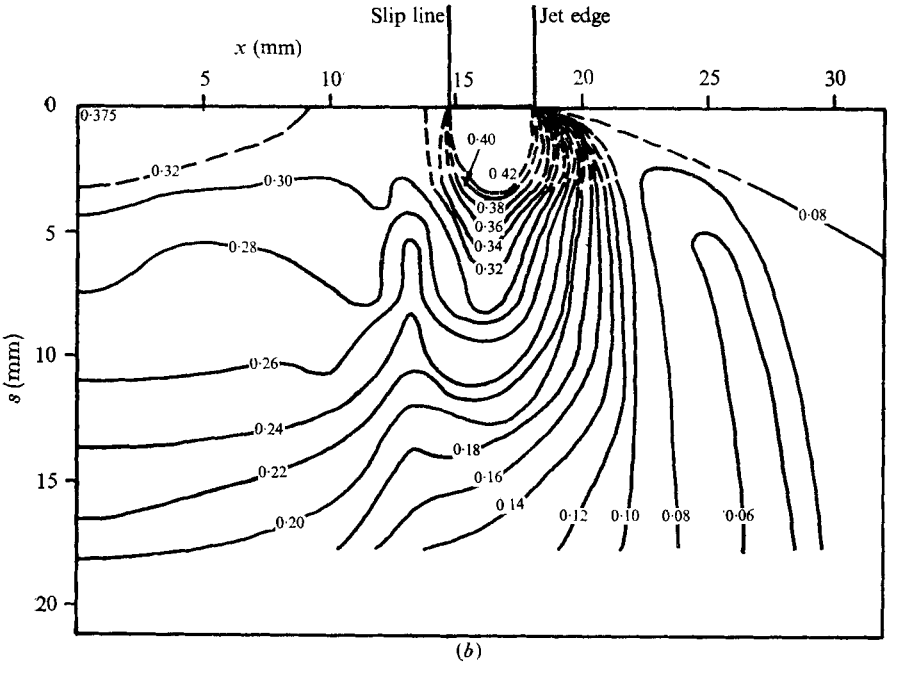

FIGURES 15(*a*), (*b*). For legend see p. 326.

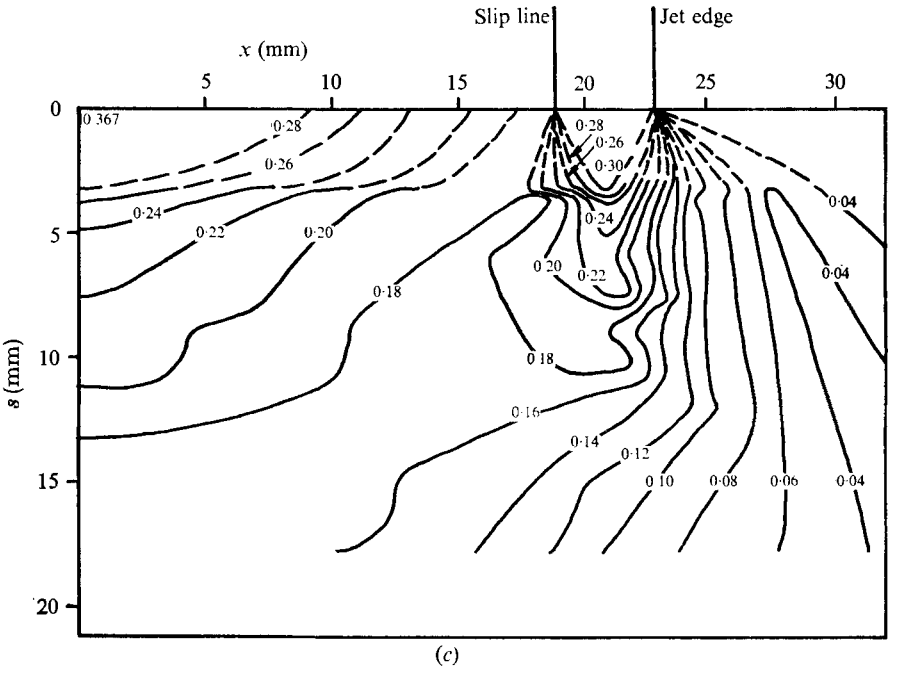

(*c*)

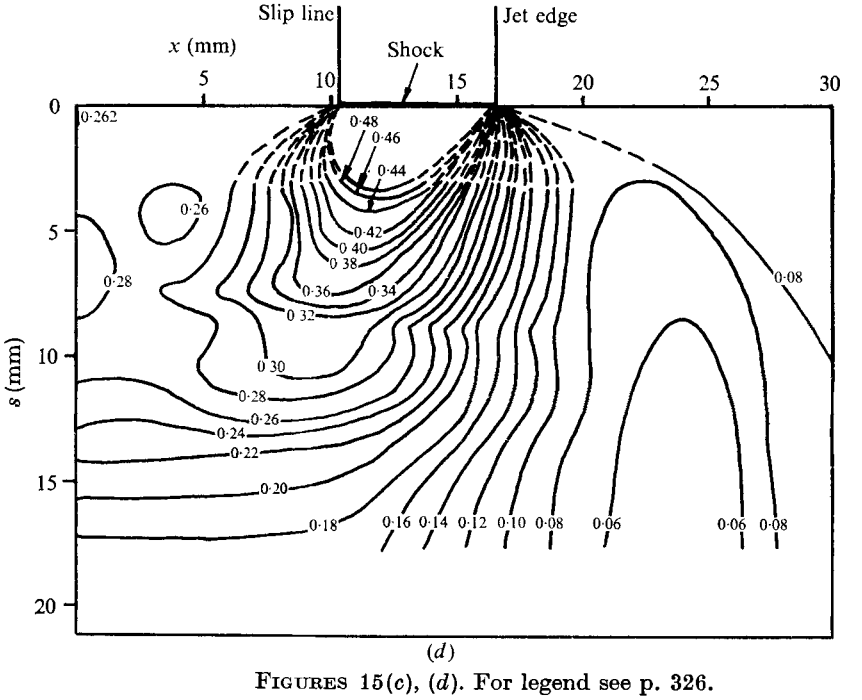

(*d*)

FIGURES 15(*c*), (*d*). For legend see p. 326.

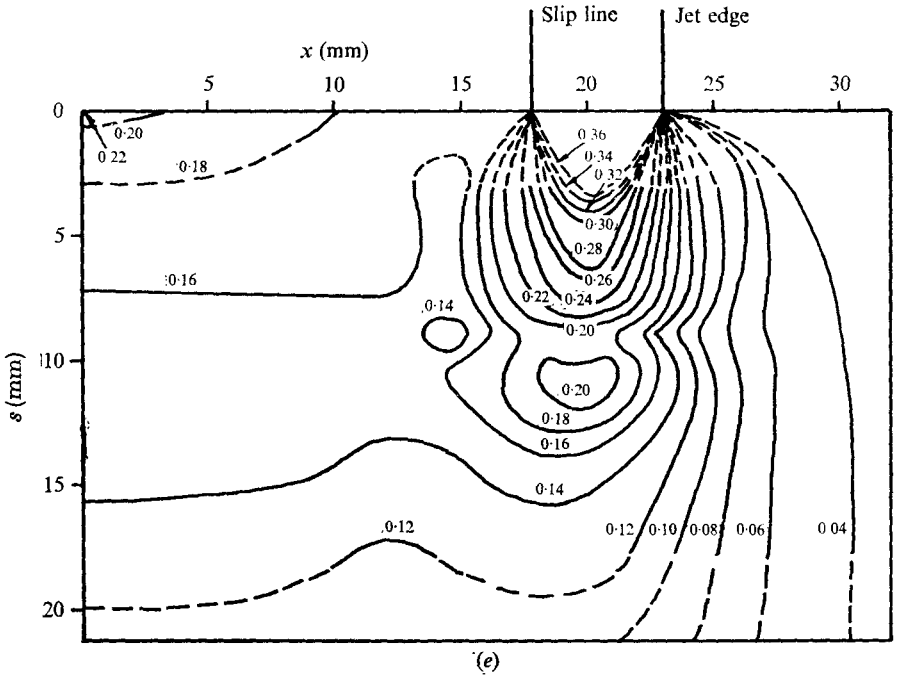

FIGURE 15. Contours of surface pressure p/p_0 for the 90° wedge below the convergent–divergent nozzle. (*a*) $z_w = 0$, $p_e/p_a = 1{\cdot}2$. (*b*) $z_w = D_E$, $p_e/p_a = 1{\cdot}2$. (*c*) $z_w = D_E$, $p_e/p_a = 2$. (*d*) $z_w = 2D_E$, $p_e/p_a = 1{\cdot}2$. (*e*) $z_w = 2D_E$, $p_e/p_a = 2$.

The pressure peaks referred to above are produced by fluid which has come through the outer regions of the jet, where the stagnation pressure is high; this can be clearly seen from the close relationship between the locations of the peaks and of the features taken from the shadowgraphs. This also explains why no peaks occur in figures 15(*a*), 16(*a*), 17(*a*) and 18(*a*) since these are zero-separation cases and no jet shock exists in the exit plane. In order to confirm this interpretation, the triple point in figure 3(*c*) (plate 1) was analysed, using a jet shock angle measured from the figure. The stagnation pressure on the tail shock side of the slip line was calculated to be about 0·52 times the supply chamber pressure, compared with a measured peak value of 0·43 and a centre-line Pitot value of 0·375 (see figure 15*b*). It is to be expected that the peak measured value will be significantly below the outer flow stagnation pressure since the first surface tapping is some distance from the apex and it can be seen from figure 15(*b*) that the outer fluid accelerates rapidly down the wedge. Similar results were obtained for other detached-shock cases.

The impingement of a shock on the wedge occurs within the measuring section only in the cases shown in figures 16(*a*), 17(*a*) and 17(*b*). The first and second of these are transmitted shocks. The pressure rises produced can be seen on the contour plots. It can also be seen that these regions decrease in size and finally disappear as they follow the wedge shock/jet shock intersection point up towards the apex. Figure 17(*b*), on the other hand, corresponds to a double triple point

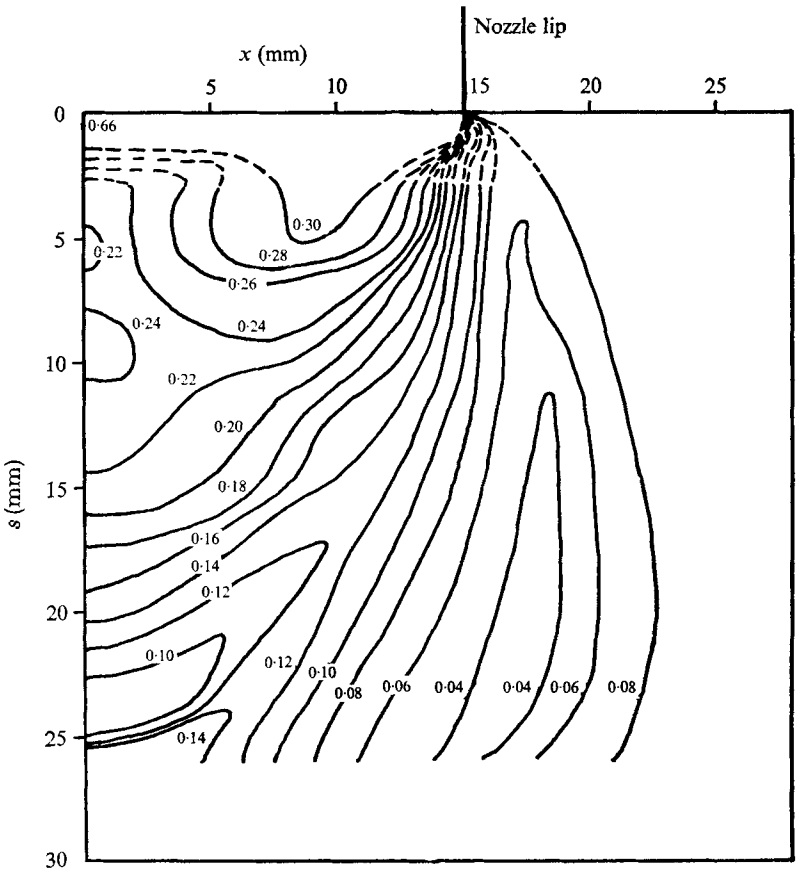

FIGURE 16(*a*). For legend see p. 329.

flow. Here the high pressure region runs almost parallel to the apex and merges with the outer flow as it streams down from the apex.

The surface pressure distributions obtained with the convergent nozzle are very similar to those measured on the same wedge with the convergent–divergent nozzle. Thus figure 18(*c*) may be compared with figure 15(*d*), while the contours in figure 18(*b*) have a very similar structure to those in figure 15(*b*). Even in the zero-spacing case, the contours in figure 18(*a*) have much the same form as those in figure 15(*a*). It should be realized, however, that the apex pressures on figure 18(*a*) are much larger than those on figure 15(*a*) because of the lower nozzle Mach number and because the gradients are much steeper: indeed, the contours are so closely spaced that it was necessary to double the interval in contour values on figure 18(*a*) compared with the value used in all the other plots.

5.4. *Flows with anomalous pressure distributions*

It was noted in § 5.2 that, in the four cases where the wedges were placed below the free-jet Mach disk, the values recorded by the apex pressure tappings did not agree with the free-jet Pitot pressures measured at the centres of the stand-off

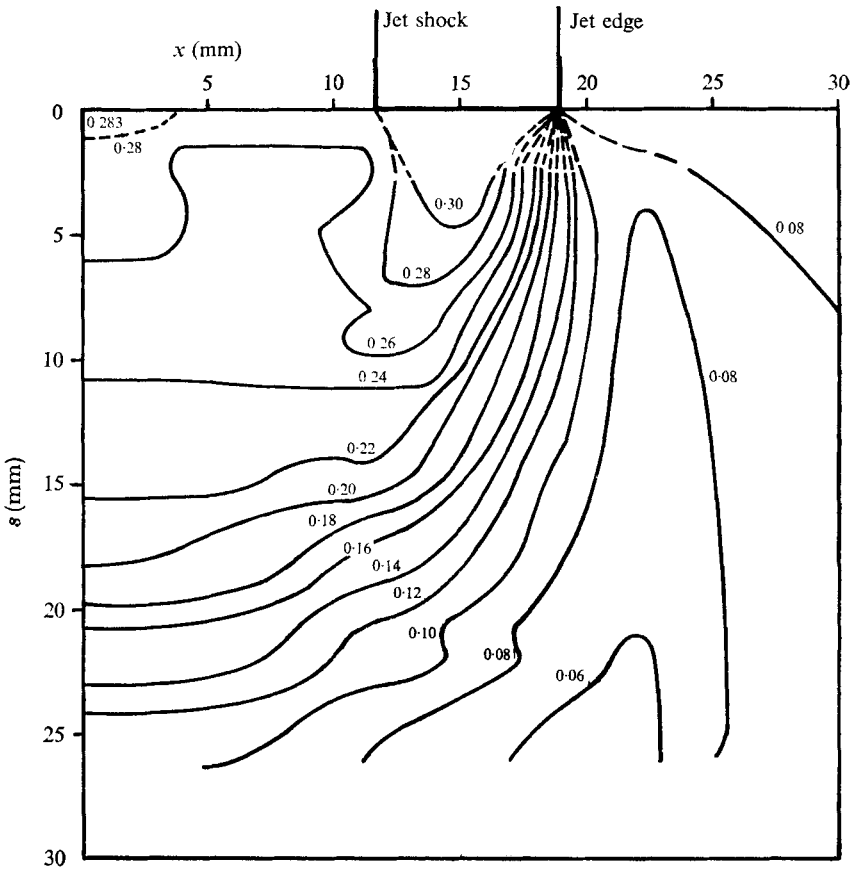

FIGURE 16(*b*). For legend see p. 329.

shock waves. Three of the centre-line pressure distributions have been plotted together in figure 13 and the fourth may be seen in figure 14. It can be seen that in each case the apex pressure is less than the free-jet Pitot pressure p_{01} and that the pressure rises to a maximum some way down the wedge. This type of pressure distribution is reminiscent of those seen where a shock layer stagnation bubble exists during impingement on a perpendicular flat plate, as reported by Ginzburg *et al.* (1970), by Donaldson & Snedeker (1971) and by Carling & Hunt (1974). In the flat-plate case, the central streamline flows over the bubble and subsequently attaches to the plate. The pressure peak occurs approximately at the attachment point and has a value a little less than the centre-line Pitot pressure. Now the peak pressures of the curves shown in figures 13 and 14 are substantially greater than the corresponding free-jet Pitot pressures, so that the streamline in this region cannot have originated on the centre-line. However, streamlines which originate outside the central shock have substantially higher stagnation pressures: simple analysis of the triple points gives non-dimensional values for the outer-region stagnation pressure for the convergent–divergent nozzle of about 0·58. The peak pressures on the wedge centre-line with this nozzle all have values close

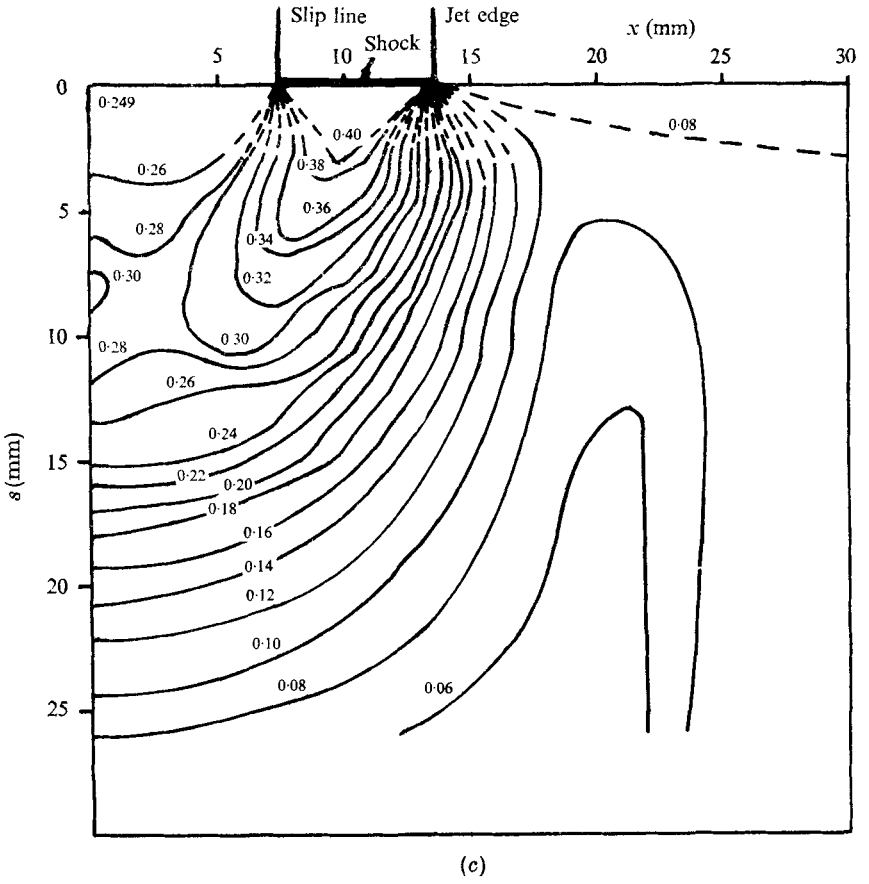

FIGURE 16. Contours of surface pressure p/p_0 for the 60° wedge below the convergent–divergent nozzle with $p_e/p_a = 1{\cdot}2$. (*a*) $z_w = 0$. (*b*) $z_w = D_E$. (*c*) $z_w = 2D_E$.

to 0·30; they can, therefore, be produced by outer-region fluid after suitable losses.

There are two ways in which flow from the outer regions can reach the wedge surface on the centre-plane. In the first, the fluid of high total pressure comes from the outer region of the jet in that plane of symmetry which is perpendicular to the wedge. Normally, the inner flow lies between this fluid and the wedge surface, but if the inner fluid were to move outwards along the wedge away from the plane of symmetry, this would enable the outer flow to approach the surface and raise the pressure either directly or by mixing with the remnants of the inner flow. There are two objections to this model. First, there is no evidence in any of figures 3(*f*), 4(*d*), 5(*d*) or 6(*d*) (plates 2, 4, 6 and 8) of an inward movement of the outer flow nor of the shock wave which one would expect on the attachment of the supersonic outer flow. Second, it would seem likely that the central apex pressure reading would be equal to the centre-line Pitot pressure since there does not seem to be any reason why a stagnation bubble should occur, although one cannot be entirely ruled out.

The second flow model is illustrated in figure 19. The fluid of high total pressure

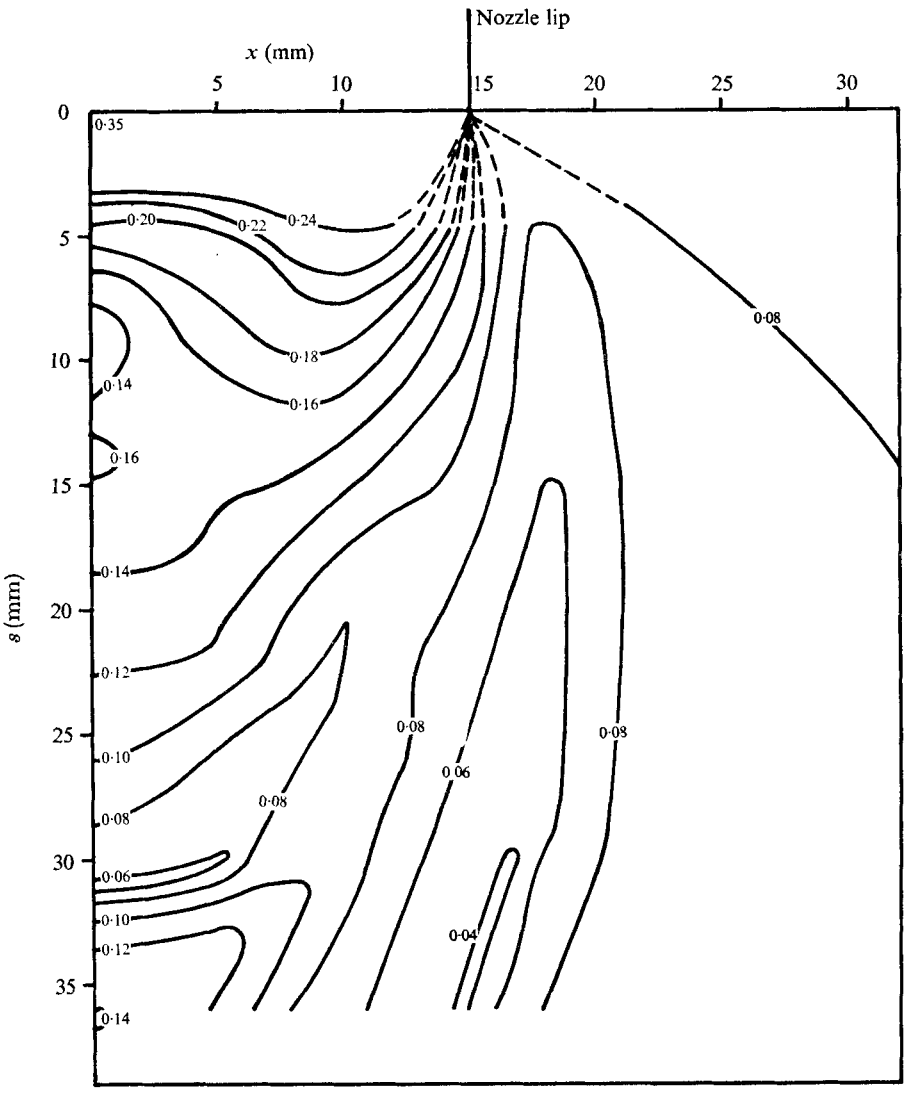

FIGURE 17(*a*). For legend see p. 332.

now comes from the outer regions of the flow in the apex plane. It streams inwards over the wedge surface towards the centre-line, where it acts as a barrier to the inner flow, which is therefore forced to separate from the surface and to flow over the top of the outer flow. This process is assisted by the presence of a stagnation bubble, which is therefore plausible in this model. If the flow field just described is correct, the inward movement of the high pressure regions should be visible in the surface pressure distributions. Examination of figures 15(*d*), 16(*c*), 17(*c*) and 18(*c*) confirms that this does happen, whereas in figure 15(*e*), for example, which is a detached-shock case with no bubble, the higher pressure contours show no inward movement.

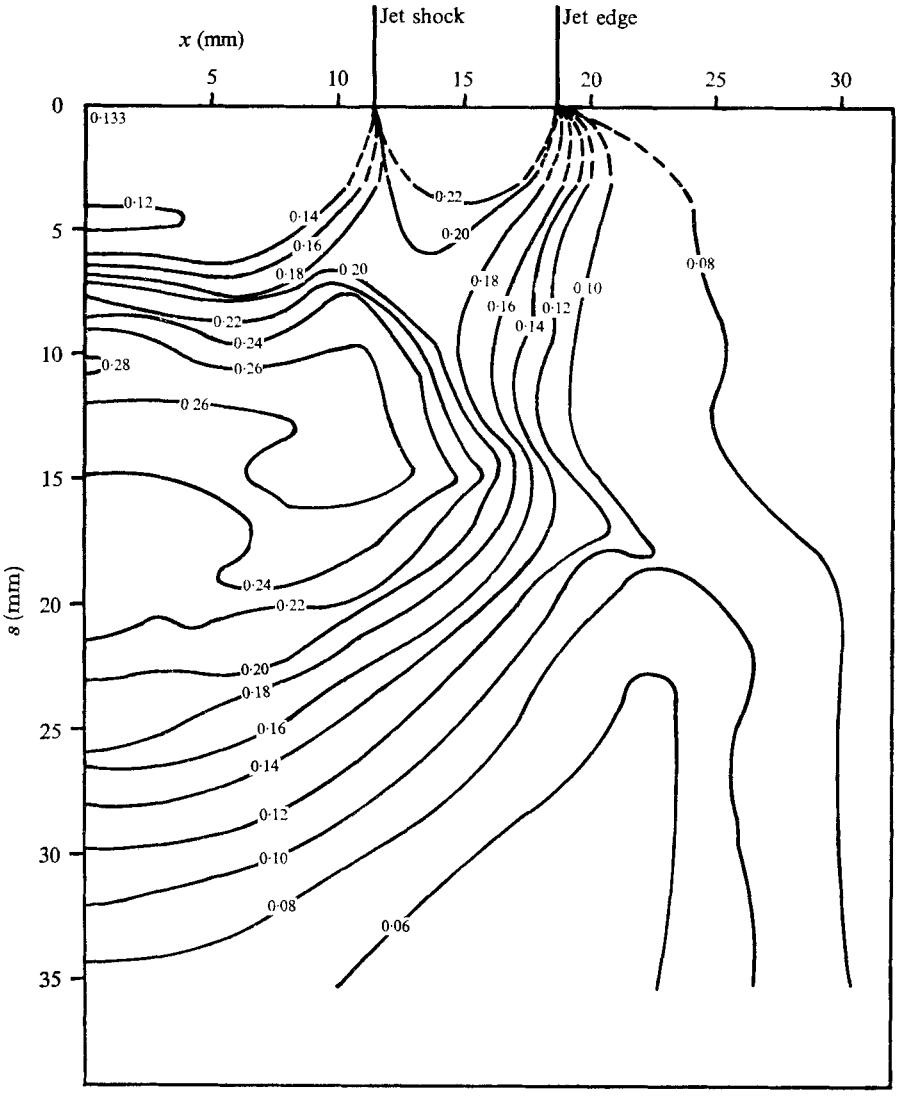

FIGURE 17(*b*). For legend see p. 332.

Surface flow-visualization tests were carried out on the 60° and 45° wedges in an attempt to confirm the second flow model. The medium used was Dayglo pigment mixed with lubricating oil; the flow patterns were subsequently photographed under ultra-violet light. It was somewhat difficult to obtain a significant deposit in the region of interest. Nonetheless, the photograph for the 45° wedge is presented in figure 20 (plate 11) and clearly shows the inward flow from the outer regions of the jet at the apex; the extent and position of these regions has been measured on figure 5(*e*) (plate 6) and is shown on figure 20. The apparent upper limit to the merging at the centre-line of the inward moving streams also agrees well with the position of the pressure peak on the curve in figure 13.

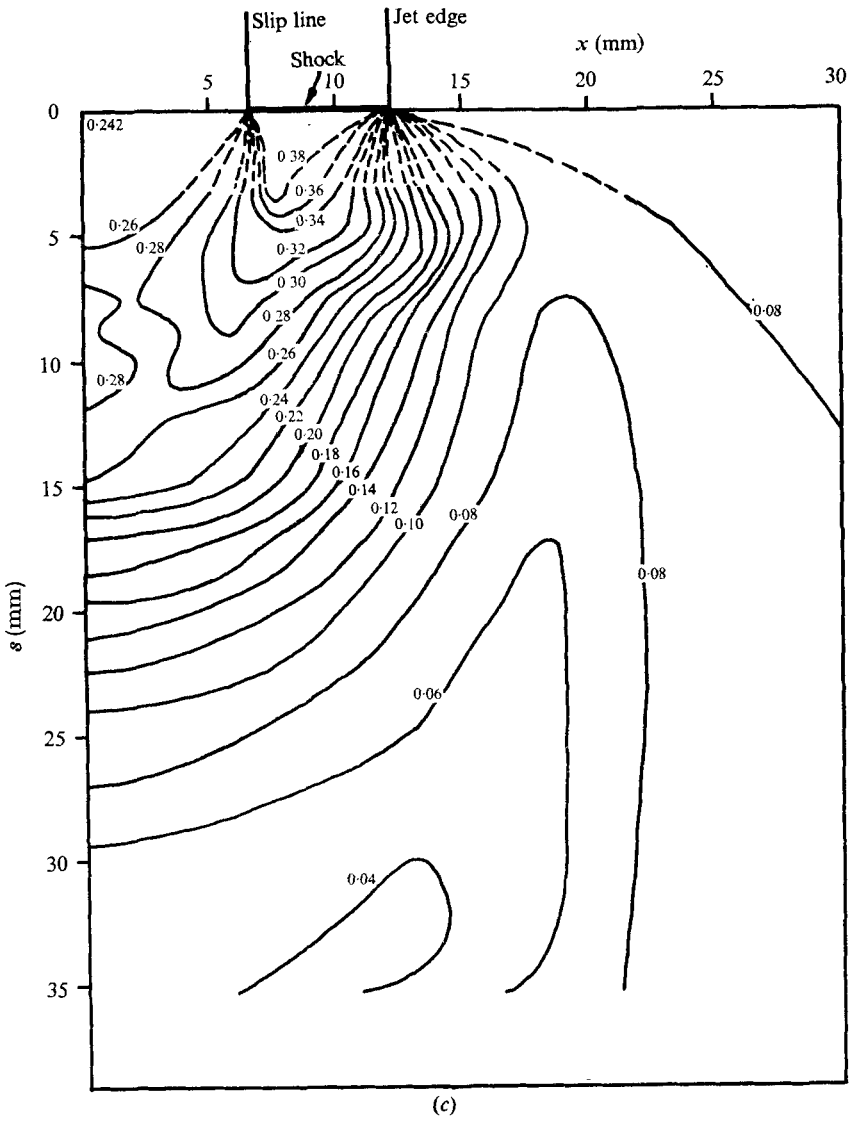

FIGURE 17. Contours of surface pressure p/p_0 for the 45° wedge below the convergent–divergent nozzle with $p_e/p_a = 1{\cdot}2$. (*a*) $z_w = 0$. (*b*) $z_w = D_E$. (*c*) $z_w = 2D_E$.

The reason why this type of flow should occur in these cases is not completely clear but the following gives a partial explanation. The common factor, that all these wedges are below the free-jet Mach disk, is probably not in itself significant. More important are the facts that the jet shock is relatively strong where it intersects the wedge shock and that the intersection point is at a relatively small radial distance. The importance of the strength of the jet shock is that the tail shock flow from the triple point is then significantly supersonic; see Kalghatgi & Hunt (1975). The supersonic tail shock flow therefore passes through a further shock wave on encountering the wedge, as can be seen in figures 3(*g*), 4(*e*), 5(*e*)

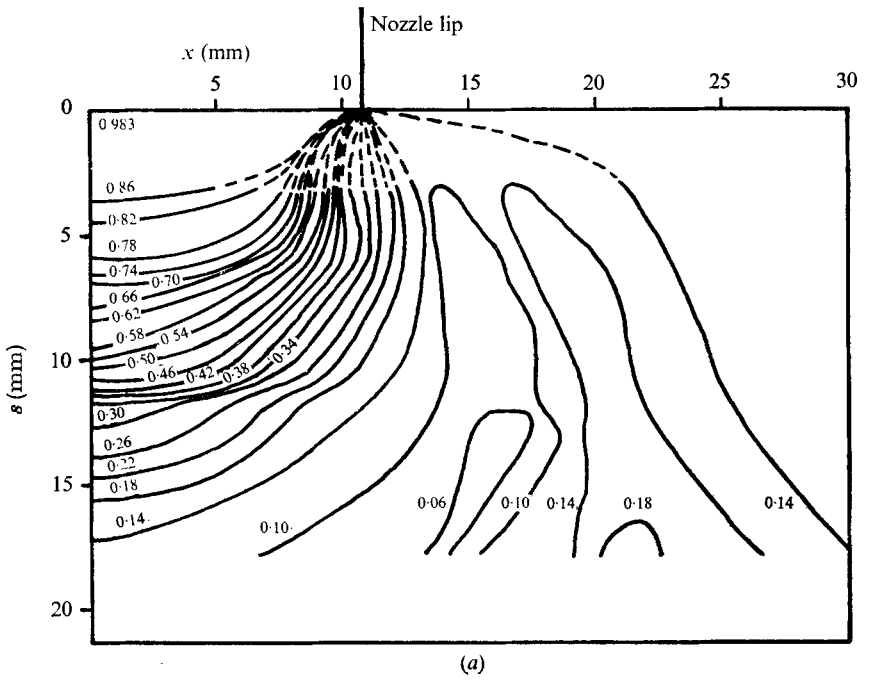

(*a*)

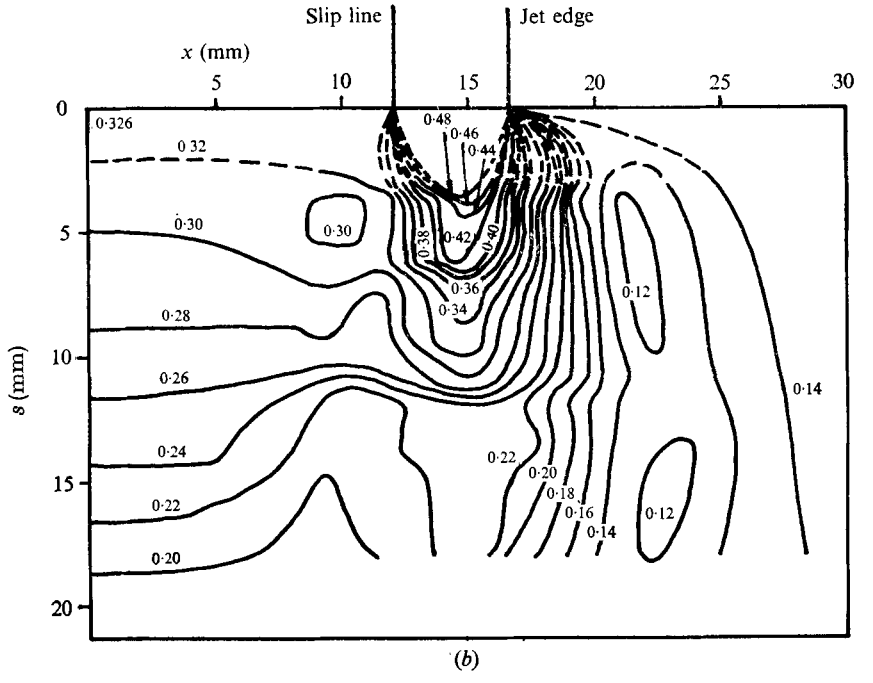

(*b*)

FIGURES 18(*a*), (*b*). For legend see p. 334.

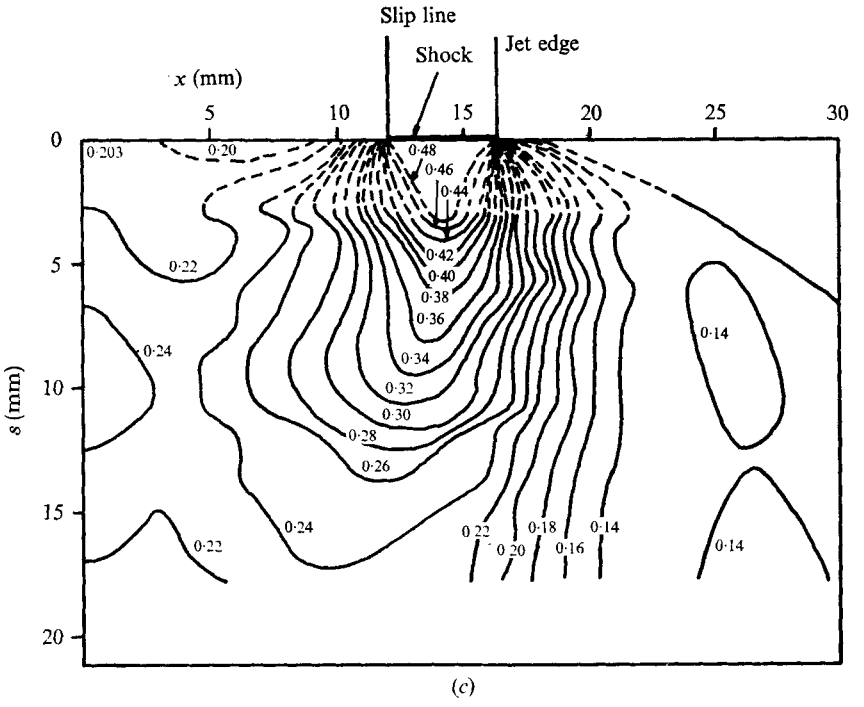

FIGURE 18. Contours of surface pressure p/p_0 for the 90° wedge below the convergent–nozzle with $p_e/p_a = 4$. (*a*) $z_w = 0$. (*b*) $z_w = D_E$ (where D_E is the exit diameter of the convergent–divergent nozzle). (*c*) $z_w = 2D_E$.

and 6(*e*) (plates 2, 4, 6 and 8). There must therefore be a sudden pressure rise where this shock wave meets the slip line between the outer and inner flows; this jump in pressure will be alleviated in turn by an expansion fan and the flow will be deflected inwards towards the centre-line. Thus, if the inward turning is sufficient and the distance from the centre-line is not too great, the outer flow penetrates to the centre-line and establishes the flow field described above.

6. Conclusion

An initial study of the impingement of supersonic jets on wedges has been carried out. Complete front-face pressure distributions have been obtained for cases covering a range of jet conditions and wedges. Numerous shadowgraph pictures were taken.

A wide variety of flow patterns over the wedges was observed. The major factors in determining the flow pattern are the combination of centre-line Mach number, and wedge apex angle and the jet shock strength and position. Observed shock intersections agree with shock polar reconstructions of those intersections but double triple point structures sometimes occur when a four-shock confluence is also possible according to the shock polars. Evidence has been presented that this change in flow pattern is produced by an interaction involving the shock structure generated by a boundary-layer separation shock and the transmitted

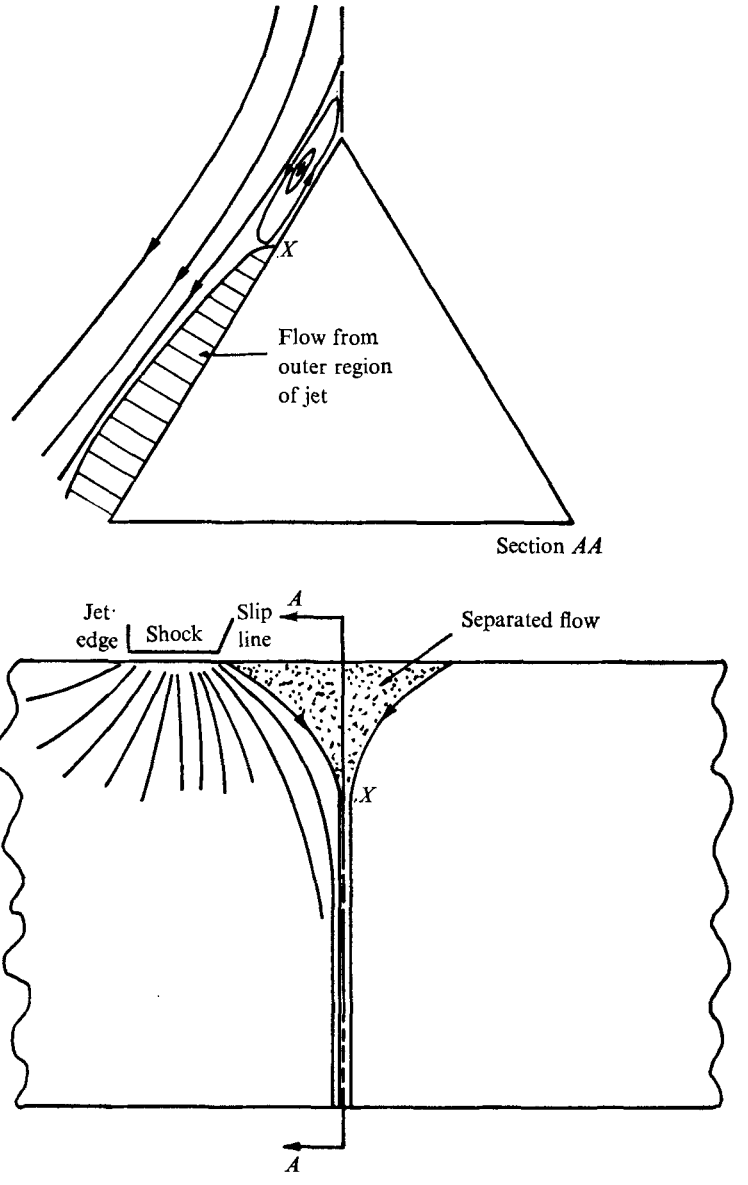

FIGURE 19. Sketch of the suggested flow pattern in the anomalous cases.

part of the jet shock. The study of this flow has disclosed the existence of the hitherto unobserved β triple shock confluence. An interesting and unusual flow pattern has been observed and described.

This work has been carried out with the support of the Procurement Executive, Ministry of Defence. Thanks are also due to Mr D. Cairns (British Aircraft Corporation), Mr R. E. Jarvis (Ministry of Defence) and Mr A. Wilson (Rocket Propulsion Establishment) for their interest and encouragement.

REFERENCES

BELOV, I. A., GINZBURG, I. P. & SHUB, L. I. 1973 *Int. J. Heat Mass Transfer*, **16**, 2067.

CARLING, J. C. & HUNT, B. L. 1974 *J. Fluid Mech.* **66**, 159.

DONALDSON, C. DUP. & SNEDEKER, R. S. 1971 *J. Fluid Mech.* **45**, 281.

EDNEY, B. 1968 *Aero. Res. Inst. Sweden FFA Rep.* no. 115.

GINZBURG, I. P., SEMILETENKO, B. G., TERPIGOREV, V. S. & USKOV, V. N. 1970 *J. Engng Phys. U.S.S.R.* **19**, 412.

HENDERSON, L. F. 1965 *Aero. Quart.* **16**, 42.

KALGHATGI, G. T. & HUNT, B. L. 1975 *Aero. Quart.* **26**, 117.

PACK, D. C. & ROBERTS, L. 1953 *Phil. Mag.* **44**, 352.

SHIFRIN, E. G. 1969 *Fluid Dyn.* **4**, 70.

SHIFRIN, E. G. 1972 *Fluid Dyn.* **7**, 687.

VICK, A. R., ANDREWS, E. H., DENNARD, J. S. & CRAIDON, C. B. 1964 *N.A.S.A. Tech. Note*, D-2327.

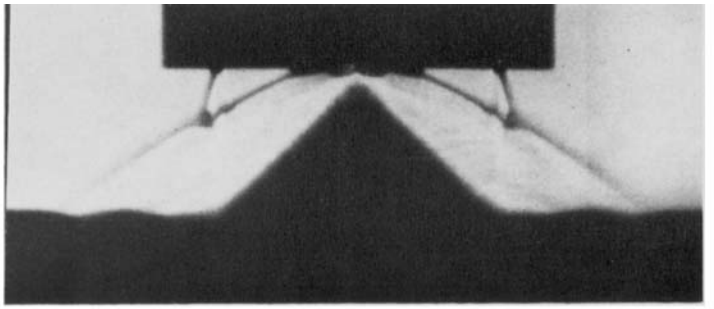

(*a*)

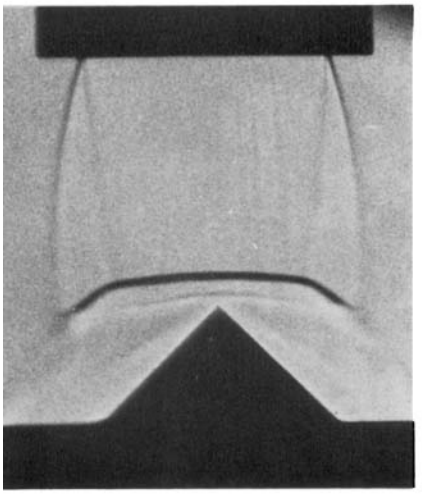

(*b*)

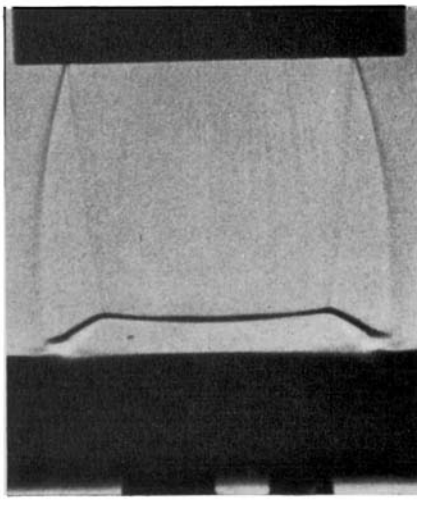

(*c*)

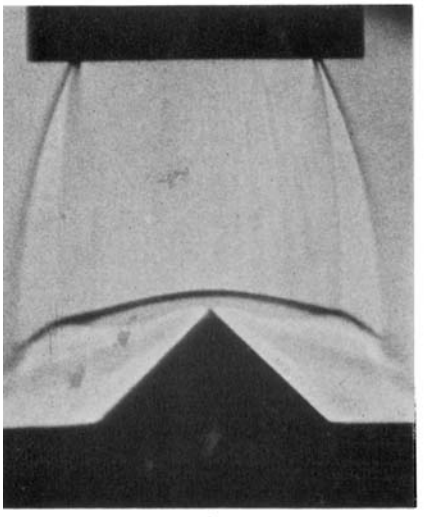

(*d*)

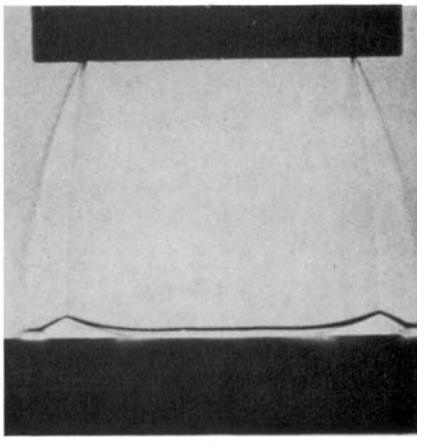

(*e*)

FIGURES 3(*a*)–(*e*). For legend see plate 2.

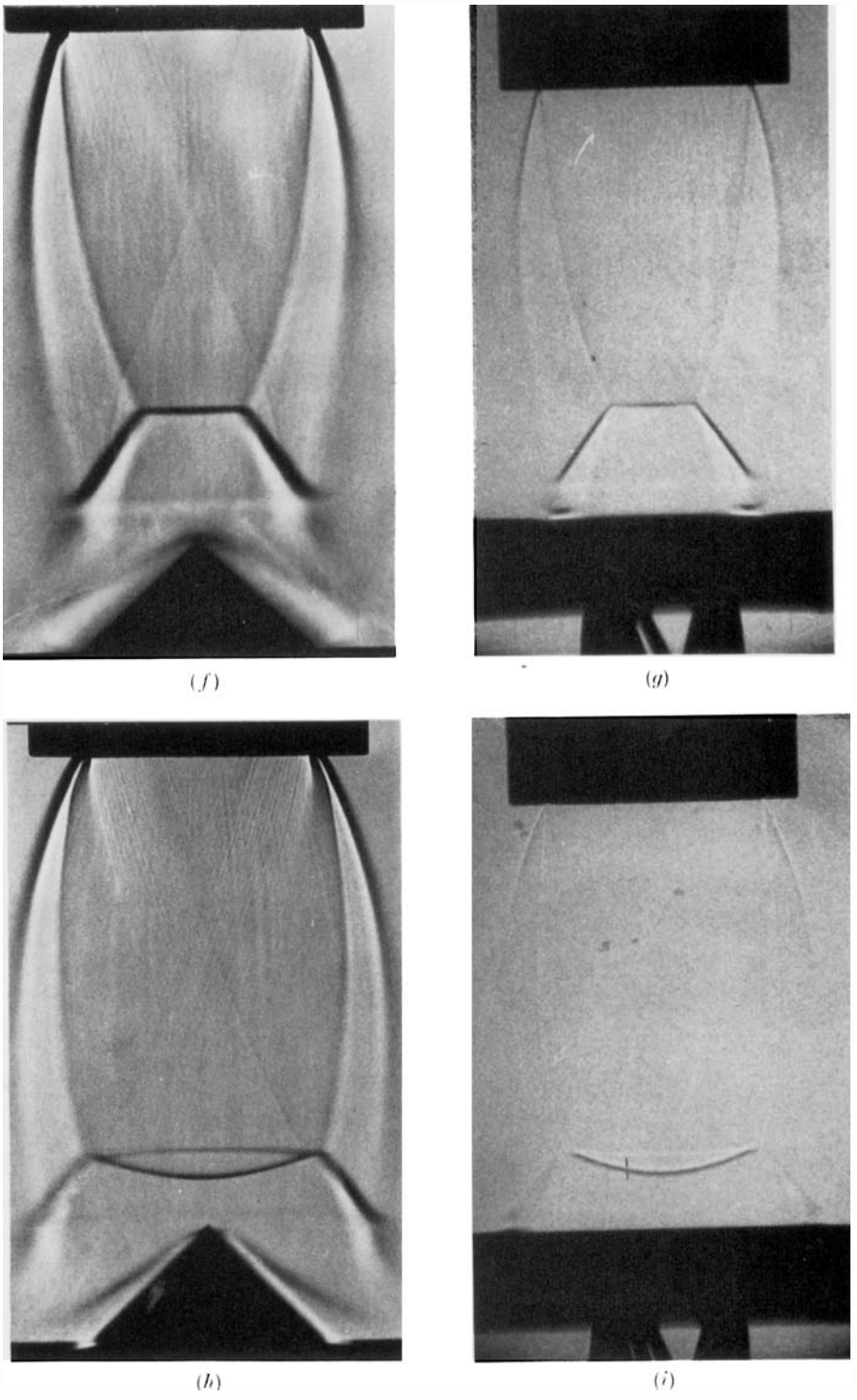

FIGURE 3. Shadowgraph pictures of the 90° wedge below the convergent-divergent nozzle. (*a*) $z_w = 0$, $p_e/p_a = 1{\cdot}2$. (*b*) $z_w = D_E$, $p_e/p_a = 1{\cdot}2$. (*c*) $z_w = D_E$, $p_e/p_a = 1{\cdot}2$, side elevation. (*d*) $z_w = D_E$, $p_e/p_a = 2$. (*e*) $z_w = D_E$, $p_e/p_a = 2$, side elevation. (*f*) $z_w = 2D_E$, $p_e/p_a = 1{\cdot}2$. (*g*) $z_w = 2D_E$, $p_e/p_a = 1{\cdot}2$, side elevation. (*h*) $z_w = 2D_E$, $p_e/p_a = 2$. (*i*) $z_w = 2D_E$, $p_e/p_a = 2$, side elevation.

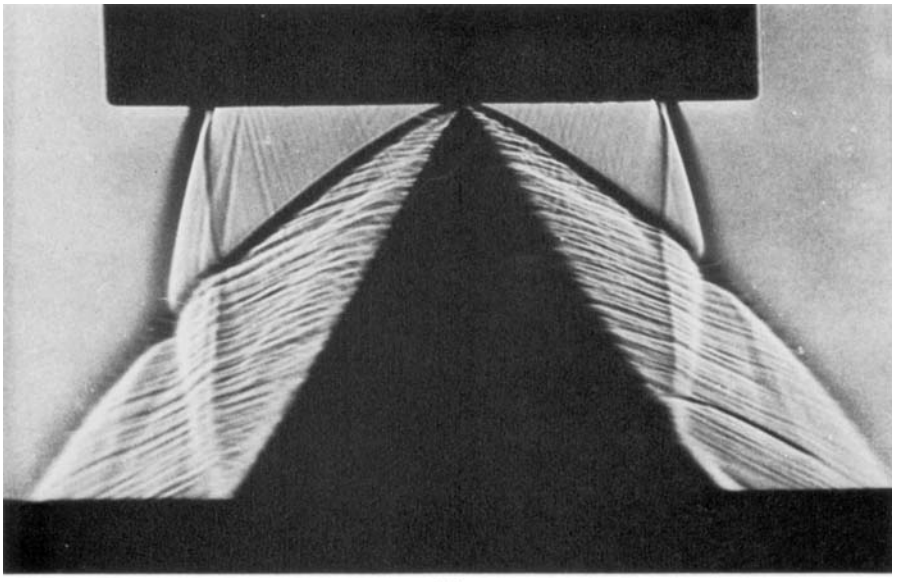

(*a*)

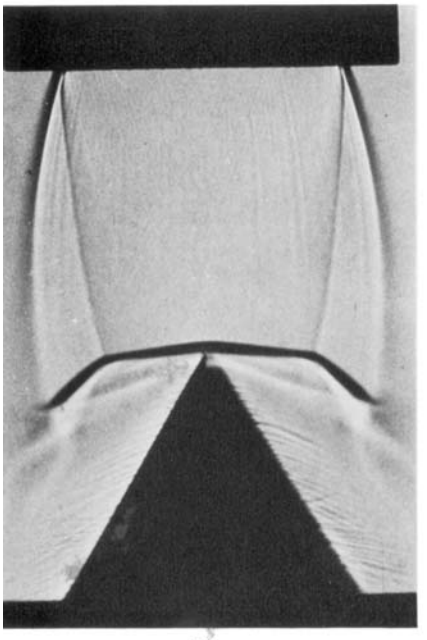

(*b*)

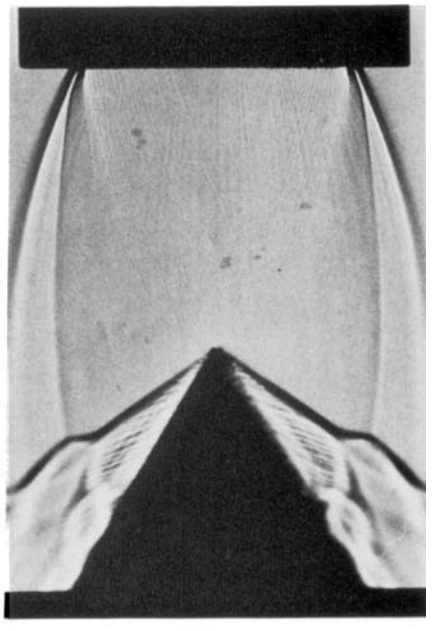

(*c*)

FIGURES 4(*a*)–(*c*). For legend see plate 4.

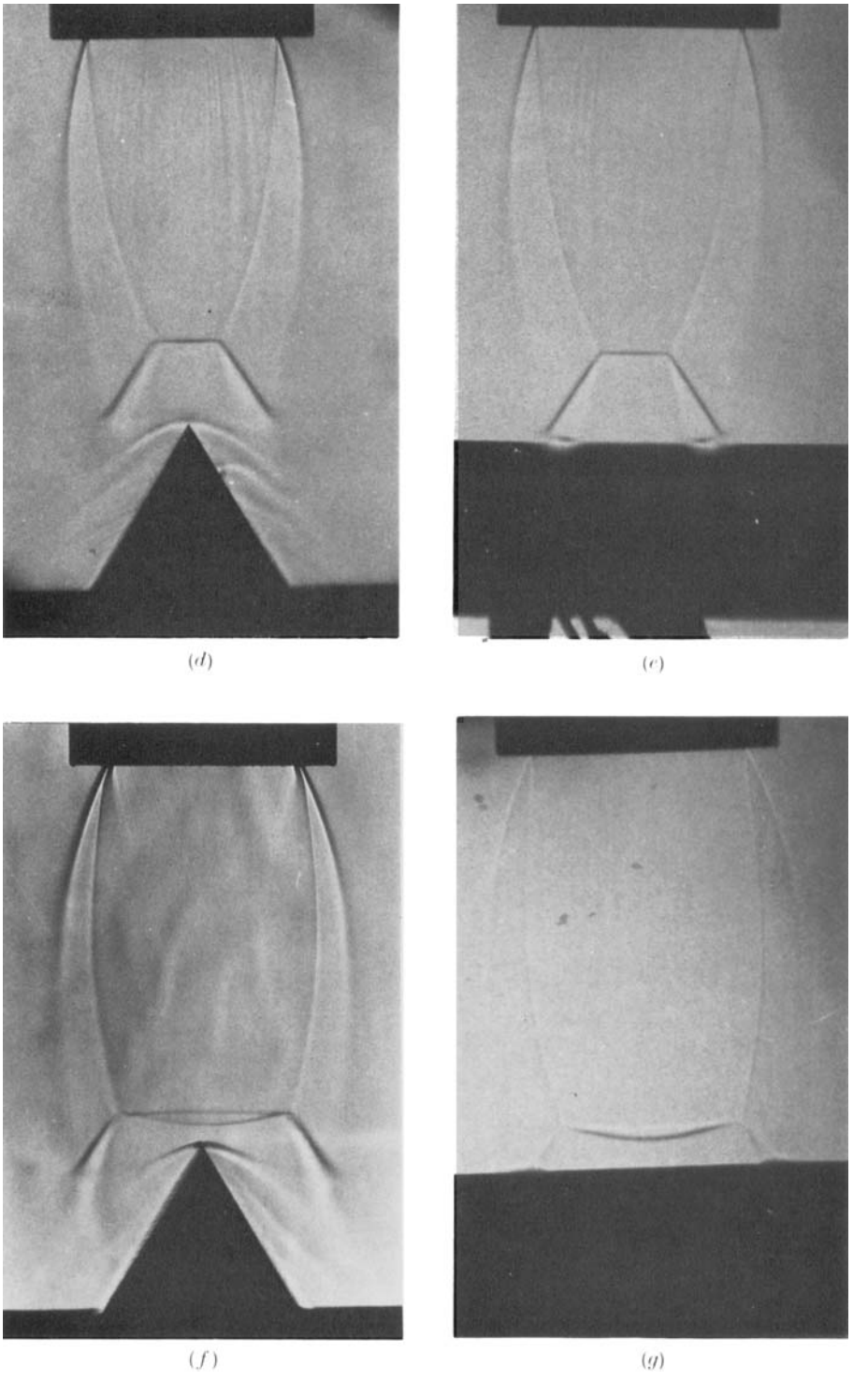

FIGURE 4. Shadowgraph pictures of the 60° wedge below the convergent–divergent nozzle. (*a*) $z_w = 0$, $p_e/p_a = 1{\cdot}2$. (*b*) $z_w = D_E$, $p_e/p_a = 1{\cdot}2$. (*c*) $z_w = D_E$, $p_e/p_a = 2$. (*d*) $z_w = 2D_E$, $p_e/p_a = 1{\cdot}2$. (*e*) $z_w = 2D_E$, $p_e/p_a = 1{\cdot}2$, side elevation. (*f*) $z_w = 2D_E$, $p_e/p_a = 2$. (*g*) $z_w = 2D_E$, $p_e/p_a = 2$, side elevation.

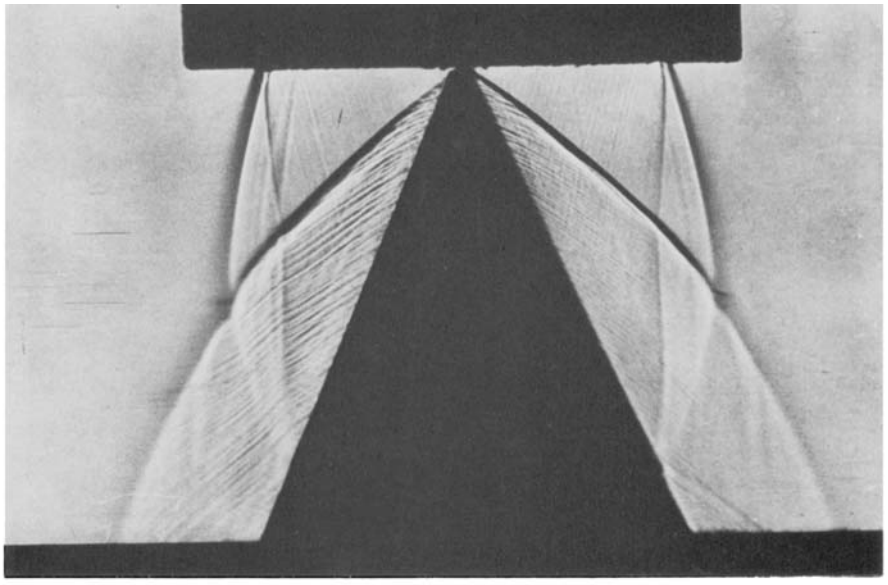

(*a*)

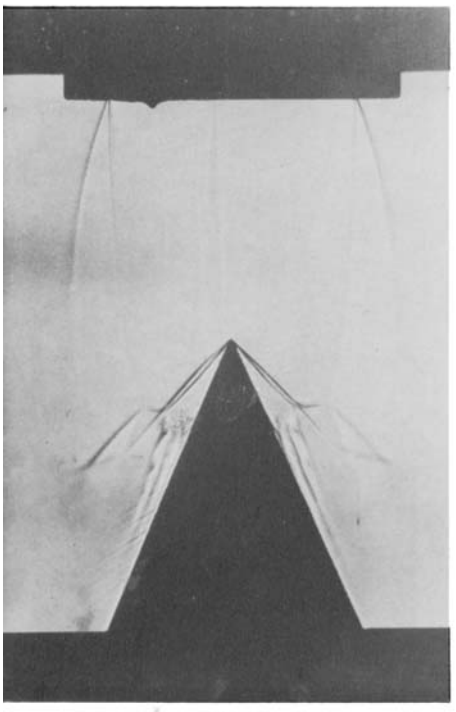

(*b*)

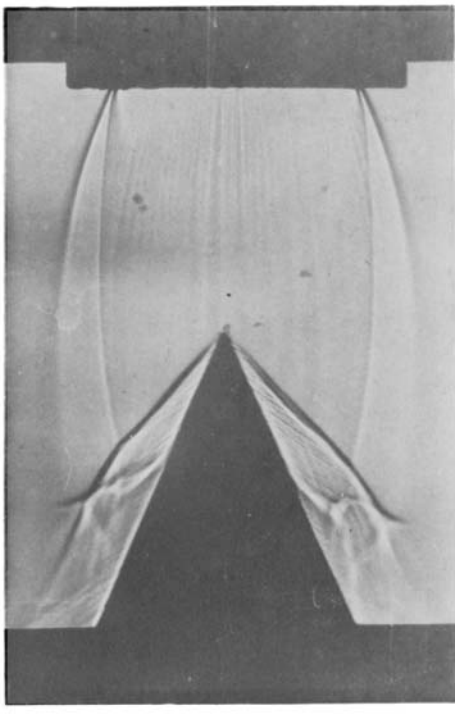

(*c*)

FIGURES 5(*a*)–(*c*). For legend see plate 6.

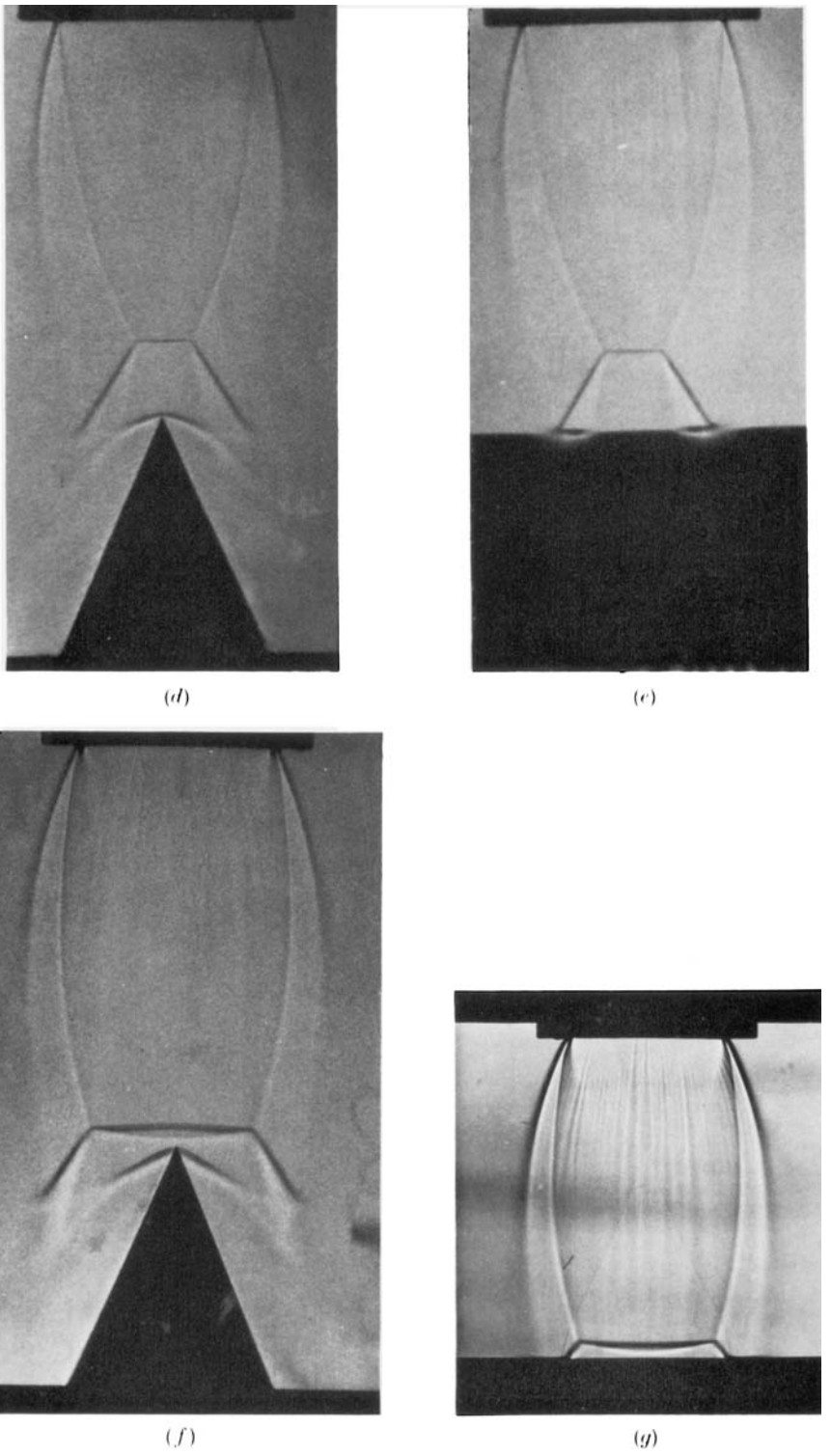

FIGURE 5. Shadowgraph pictures of the 45° wedge below the convergent–divergent nozzle. (*a*) $z_w = 0, p_e/p_a = 1{\cdot}2$. (*b*) $z_w = D_E, p_e/p_a = 1{\cdot}2$. (*c*) $z_w = D_E, p_e/p_a = 2$. (*d*) $z_w = 2D_E, p_e/p_a = 1{\cdot}2$. (*e*) $z_w = 2D_E$, $p_e/p_a = 1{\cdot}2$, side elevation. (*f*) $z_w = 2D_E$, $p_e/p_a = 2$. (*g*) $z_w = 2D_E$, $p_e/pa = 2$, side elevation.

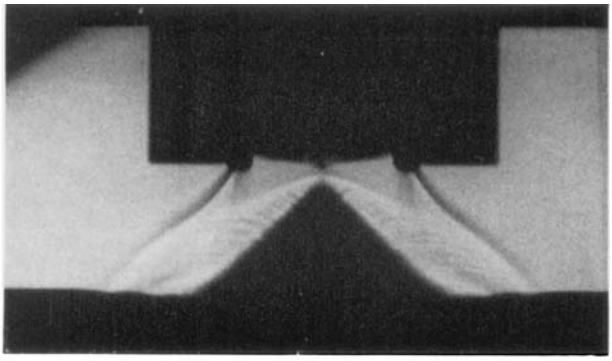

(*a*)

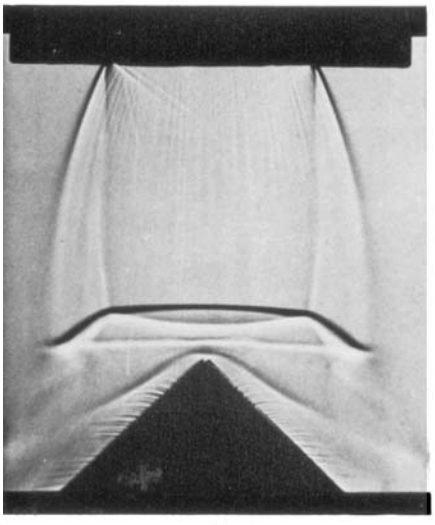

(*b*)

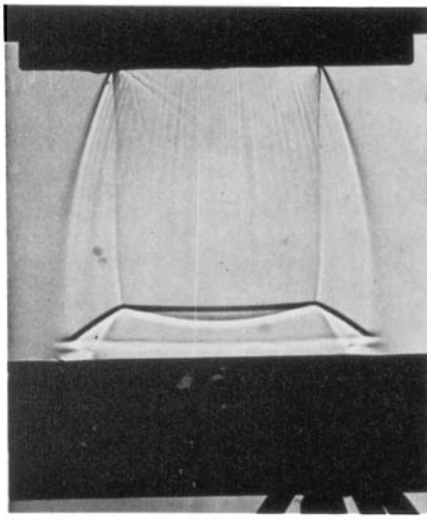

(*c*)

FIGURES 6(*a*)–(*c*). For legend see plate 8.

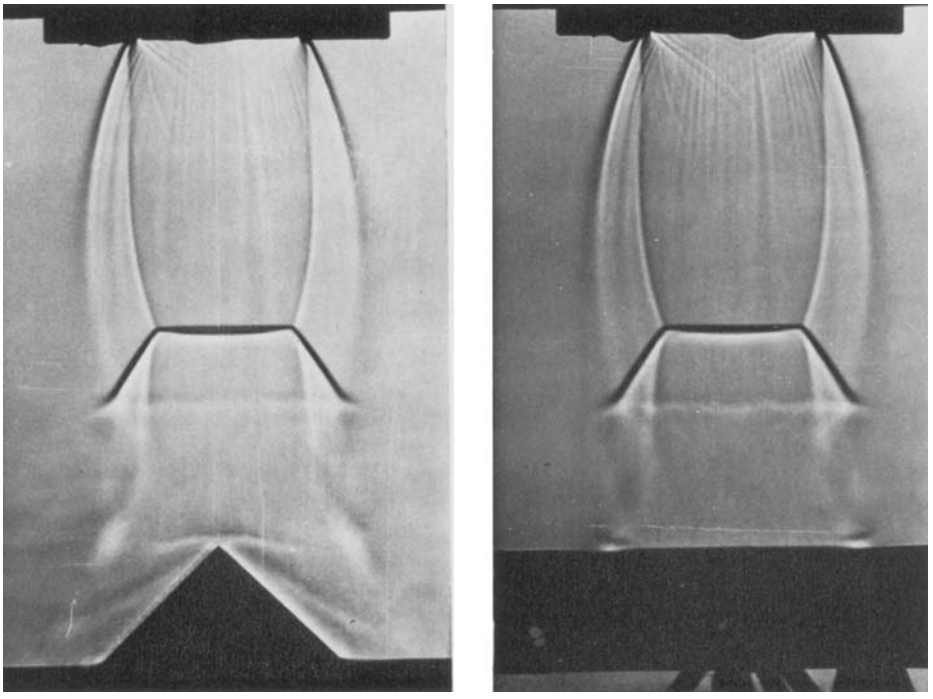

(*d*) (*e*)

FIGURE 6. Shadowgraph pictures of the 90° wedge below the convergent nozzle with $p_e/p_a = 4$. (*a*) $z_w = 0$. (*b*) $z_w = D_E$. (*c*) $z_w = D_E$, side elevation. (*d*) $z_w = 2D_E$. (*e*) $z_w = 2D_E$, side elevation.

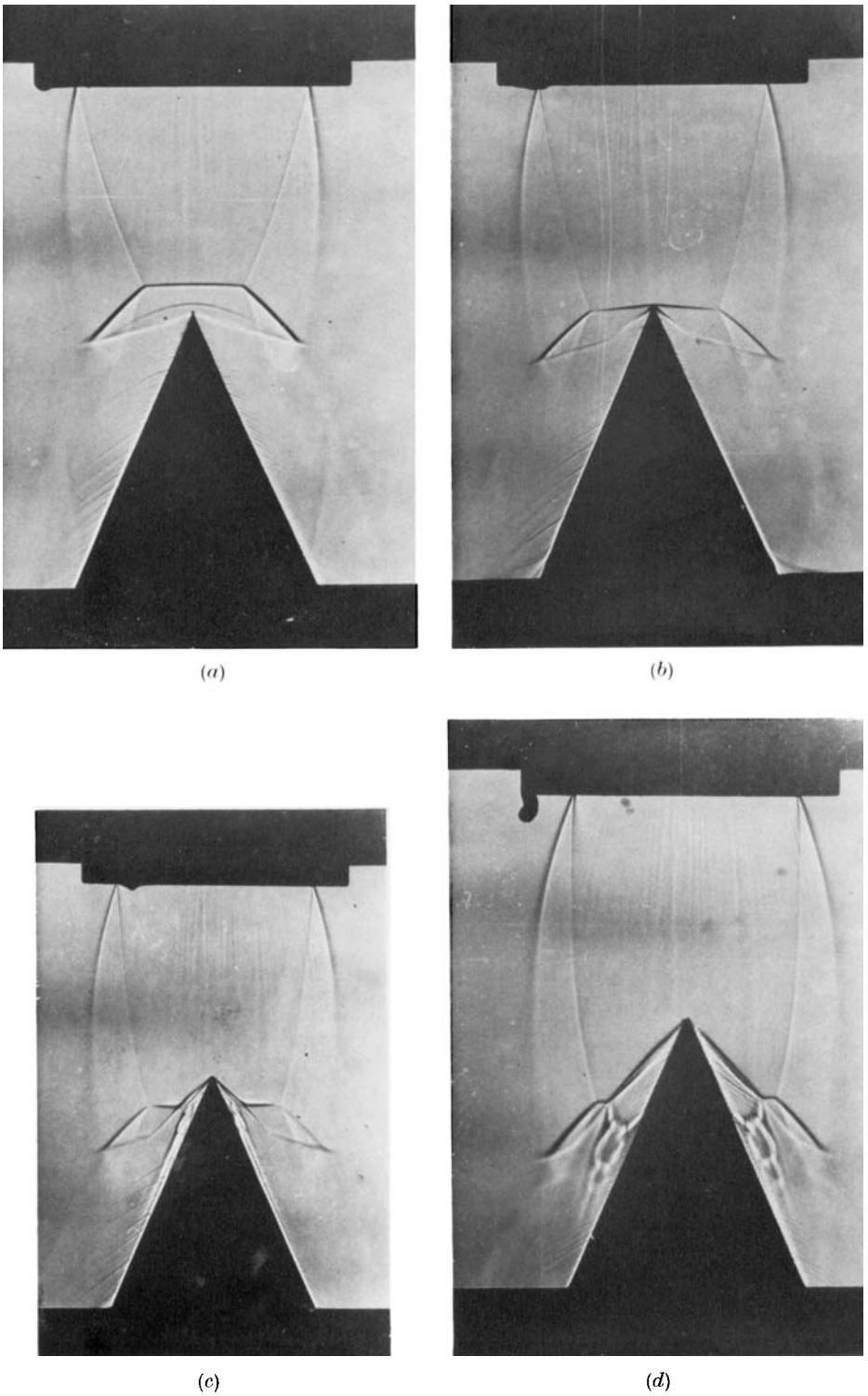

(*a*) (*b*)

(*c*) (*d*)

FIGURES 7 (*a*)–(*d*). For legend see plate 10.

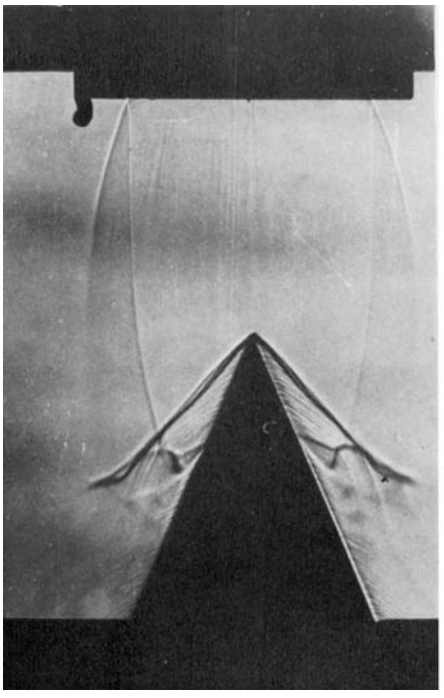

(*e*)

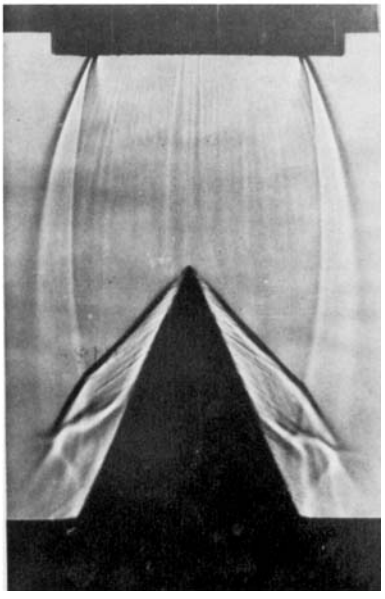

(*f*)

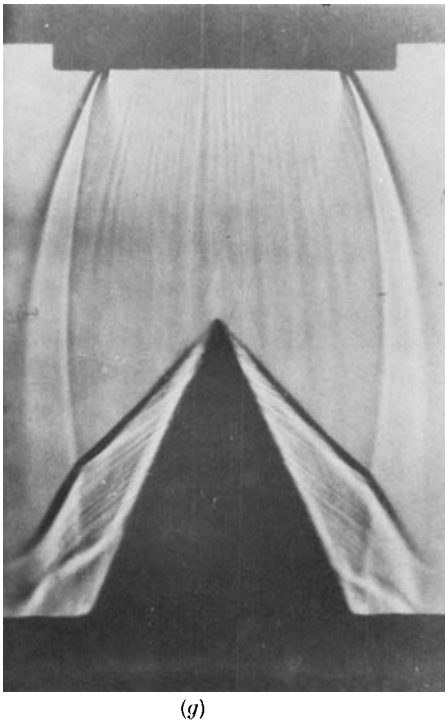

(*g*)

FIGURE 7. The effect of varying expansion ratio for the 45° wedge below the convergent–divergent nozzle with $z_w = D_E$. (*a*) $p_e/p_a = 0{\cdot}8$. (*b*) $p_e/p_a = 1{\cdot}0$. (*c*) $p_e/p_a = 1{\cdot}4$. (*d*) $p_e/p_a = 1{\cdot}5$. (*e*) $p_e/p_a = 1{\cdot}55$. (*f*) $p_e/p_a = 1{\cdot}8$. (*g*) $p_e/p_a = 2{\cdot}3$.

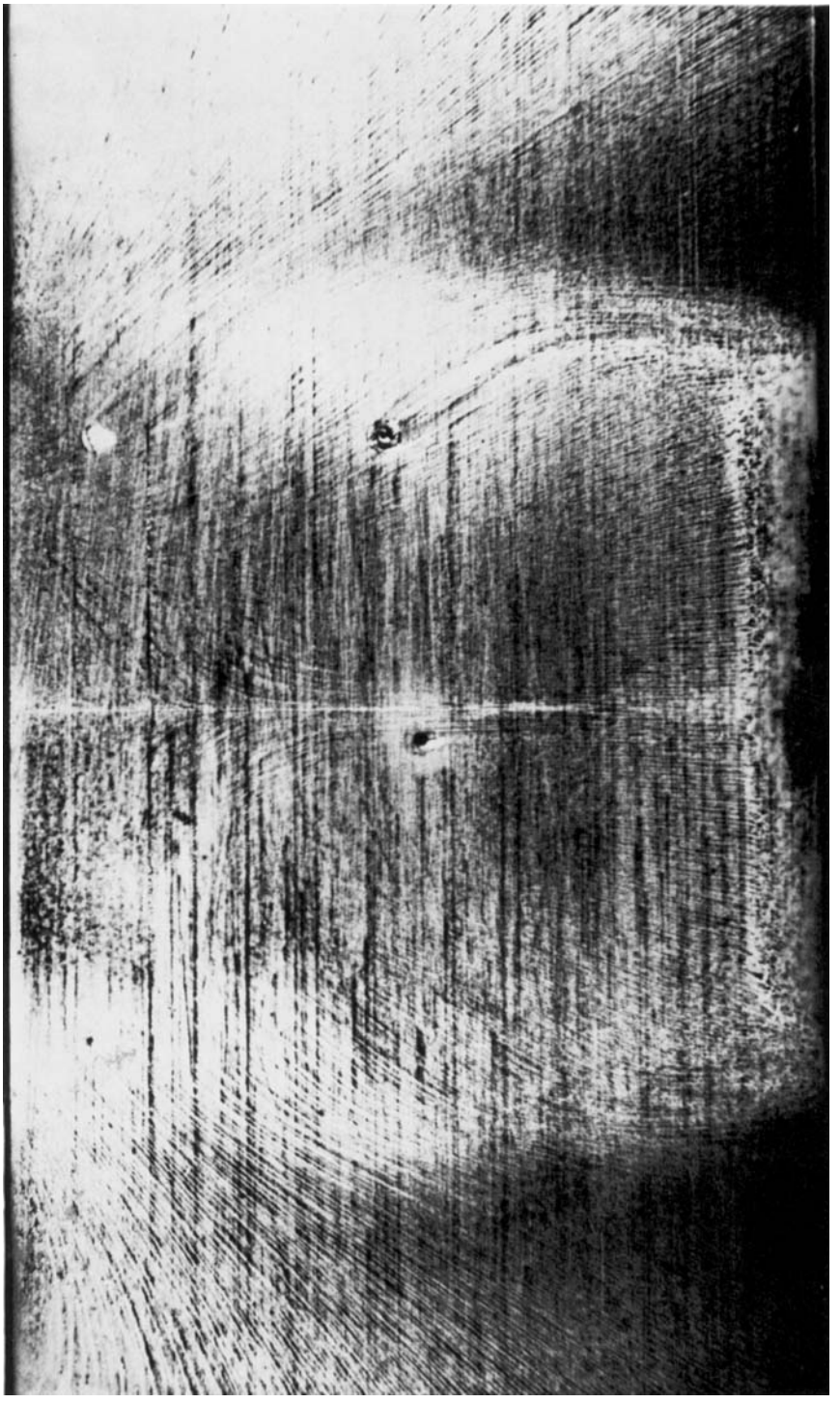

FIGURE 20. Surface flow pattern on the 45° wedge at $z_w = 2D_E$ below the convergent–divergent nozzle with $p_e/p_a = 1{\cdot}2$.